ISTANBUL BİLGİ UNIVERSITY
INSTITUTE OF GRADUATE PROGRAMS
ELECTRICAL & ELECTRONICS ENGINEERING MASTER
DEGREE PROGRAM

SELF-TUNING RESONANT MODE MICROSCANNER CONTROL SYSTEM

Ayşin Arseven
119815020

Asst. Prof. Baykal Sarıoğlu
Assoc. Prof. Yiğit Dağhan Gökdel

İSTANBUL
2023

SELF-TUNING RESONANT MODE MICROSCANNER CONTROL SYSTEM

KENDİNDEN AYARLANAN REZONANT MODLU MİKROTARAYICI KONTROL SİSTEMİ

Ayşin Arseven

119815020

APPROVED BY:

Thesis Supervisor	**:** Asst. Prof. Baykal Sarıoğlu (Istanbul Bilgi University)	.....
Thesis Co-supervisor	**:** Assoc. Prof. Yiğit Dağhan Gökdel (Istanbul Bilgi University)	.....
Member of a Jury	**:** Assoc. Prof. Onur Ferhanoğlu (Istanbul Technical University)	.....
Member of a Jury	**:** Asst. Prof. Okan Zafer Batur (Istanbul Bilgi University)	.....
Member of a Jury	**:** Asst. Prof. İbrahim Başar Aka (Istanbul Bilgi University)	.....

Date of approval: 19.04.2023

Total number of pages: 101

Keywords (English):

1) Microscanner
2) Magnetic actuation scheme
3) Planar electrocoil
4) Total optical scan angle (TOSA)
5) Piezoresistive feedback

Keywords (Turkish):

1) Mikrotarayıcı
2) Manyetik hareketlendirme şeması
3) Düzlemsel elektrobobin
4) Toplam optik tarama açısı (TOSA)
5) Piyezodirençli geri besleme

Dedicated to my family,

ACKNOWLEDGEMENTS

Master's was an important journey that taught me and helped me deepen in my field. I would like to thank my thesis advisor Baykal Sarığlu, who has been an exemplary academician and engineer for me with his consultancy, perspective, and love of doing the job, and who has not spared his support throughout my study. I would like to thank my co-advisor Yiğit Dağhan Gökdel, who is an exemplary person, academician and researcher with his perspective, approach and kind style, who did not spare his support and suggestions for me to start this path. They are open to new ideas, have a motivating style and realistic approaches. I feel lucky to be working with them.

I am happy with the result I got from my successful and satisfying thesis. The meaning and importance of doing research was reinforced during my master's degree. This path taught me to be brave, to be confident, not to stop defending what you know, to work with more determination and energy after negative results, to love the learning state and turn it into a passion. Undergraduate and graduate education were two different adventures. I enjoyed both of these adventures separately at Istanbul Bilgi University. After having the determination to research, I saw that it is possible to work in anywhere in the world. I would like to thank my mother, Ayşe Tezel, for her financial and moral support on this path, and my family elders Fatma Tezel, Meliha and Ahmet Arseven. I would like to thank my senior, Gökçe Aköz, who I worked with during my undergraduate years, who was a wonderful person with his patience and personality, who guided me to progress in my own project in her work, and Berkay Alçiçek for his support in my studies. I would like to thank the invaluable Ömer Gökalp Akcan for his moral support, his experience, patience, work discipline and love of research. I would like to thank my very dear close friend Nilay Dalkıran for her support. I am so grateful to them for always being there for me and supporting me during my high and low moods.

ABSTRACT

This thesis demonstrates design, implementation, and experimental results of a low-cost, and low-power one-dimensional two gimballed magnetically actuated scanner capable of unidirectional scanning with piezoresistive feedback system that can be used for bioscanning applications. The proposed flexible scanner structure consists of an embedded planar electrocoil with the main fabrication material polyimide. Moreover, the system ensures real-time feedback signal by means of the graphite that is coated onto the flexure for the sake of the closed-loop systems. The system is auto-tuned in order to maintain the resonant mode of the microscanner.

The slight, and flexible substrate material of the scanner reduces the energy consumption and performs as 1D-scanning. The optimization and characterization of the planar electrocoil embedded in the scanner, which activates the scanner by creating an electromagnetic field with the effect of the external magnet, has been completed. The size of the outer frame of the structure is 40 $mm \times 40$ mm, and the moving scanning surface is 15 $mm \times 14$ mm with a thickness of 150 μm. In order to maximize the amount of scanner displacement and total optical scanning angle (TOSA), the positions of the system components is optimized. Polyimide-based scanner's optical scanning angle is 73.59° in slow-scan direction at the approximately 82 Hz. Moreover, the saturation point frequency from the real-time piezoresistive feedback is approximately 81 Hz. The average error rate result is a 1.2%. The proposed scanner structure is characterized and tested in various experiments using a laser doppler vibrometer setup, and a piezoresistive feedback setup.

Key words: Microscanner, Magnetic Actuation Scheme, Planar Electrocoil, Total Optical Scan Angle (TOSA), Piezoresistive Feedback.

ÖZET

Bu tez, biyolojik tarama uygulamaları için kullanılabilecek, piezodirençli geri besleme sistemi ile tek yönlü tarama yapabilen, düşük maliyetli ve düşük güçlü, tek boyutlu, iki yalpa çemberli, manyetik olarak çalıştırılan bir tarayıcının tasarımını, uygulamasını ve deneysel sonuçlarını göstermektedir. Önerilen esnek tarayıcı yapısı, ana üretim malzemesi poliimid ile gömülü bir düzlemsel elektro bobinden oluşur. Ayrıca sistem, kapalı devre sistemler için fleksur üzerine kaplanan grafit sayesinde gerçek zamanlı geri besleme sinyali sağlamaktadır. Mikro tarayıcının rezonans modunu korumak için sistem otomatik olarak ayarlanır.

Tarayıcının hafif ve esnek alt tabaka malzemesi, enerji tüketimini azaltır ve bir boyutlu tarama gerçekleştirir. Harici mıknatısın etkisiyle elektromanyetik alan oluşturularak tarayıcıyı harekete geçiren tarayıcıya gömülü düzlemsel elektrobobin optimizasyonu ve karakterizasyonu tamamlanmıştır. Yapının dış çerçevesinin boyutu 40 mm×40 mm ve hareketli tarama yüzeyi 15 mm × 14 mm ve kalınlığı 150μm'dir. Tarayıcı yer değiştirme miktarını ve toplam optik tarama açısını (TOSA) en üst düzeye çıkarmak için sistem bileşenlerinin konumları optimize edilmiştir. Poliimid tabanlı tarayıcının optik tarama açısı, yaklaşık 82 Hz'de yavaş tarama yönünde $73,59°$'dır. Ayrıca, gerçek zamanlı piezodirençli geri beslemeden doyma noktası frekansı yaklaşık 81 Hz'dir. Ortalama hata oranı sonucu %1.2'dir. Önerilen tarayıcı yapısı, bir lazer doppler vibrometre kurulumu ve bir piezodirençli geri besleme kurulumu kullanılarak çeşitli deneylerde karakterize edilmiş ve test edilmiştir.

Anahtar kelimeler: Mikrotarayıcı, Manyetik Çalıştırma Şeması, Düzlemsel Elektro Bobin, Toplam Optik Tarama Açısı (TOSA), Piezodirençli Geri Besleme.

TABLE OF CONTENTS

LIST OF FIGURES

LIST OF TABLES

LIST OF SYMBOLS

a	Half the flexure width
A_{PR}	Cross-section of the piezoresistive layer
b	Half the flexure thickness
$\vec{B}$	Magnetic induction
d_{in}	Distance of the inner gap of planar electrocoil
E	Modulus of elasticity
F_B	Force stemming from the magnetic field
F_E	Force stemming from the electric field
F_L	Lorentz force
F_r	Resonant frequency
G	Torsional modulus
I_m	Microscanner inertia
I_p	Flexure polar moment of inertia
K_{ab}	Flexure polar moment of inertia constant
K_s	Spring constant
L_c	Length of planar electrocoil
L_{cp}	Length of the copper conductive pad
L_f	Length of the flexure beam
L_g	Length of the outer frame aperture
L_{of}	Length of the outer frame
$L_{Rectangle}$	Inductance of the rectangular planar electrocoil
L_{PR}	Length of the piezoresistive layer
L_s	Length of inner frame
N	Number of turn
q	Charge on planar coil
q_{load}	Loaded charge
R	Electrical resistance
R_{PR}	Resistance value of piezoresistive layer

t_s	Thickness of the scanner
t_c	Thickness of the copper line
V_{pp}	Peak-to-peak voltage
w_c	Width of planar electrocoil
w_{cl}	Width of the planar electrocoil copper line
w_{cp}	Width of the copper conductive pad
w_f	Width of the flexure beam
w_g	Width of the outer frame aperture
w_o	Diameter of screw hole
w_{of}	Width of the outer frame
w_p	Distance between two copper lines of planar electrocoil
w_s	Width of inner frame
ΔR	Resistance change
ΔV/V	Normalized voltage change
θ	Scanning angle
μ_0	Magnetic permeability of space
μ_r	Relative permeability of the magnetic material
v	Velocity of charge
δ_{max}	Maximum stress on the flexure
ρ	Composite density of microscanner
ρ_{PR}	Resistivity of the piezoresistive material
ρ_{wire}	Resistivity of the copper
σ_{max}	Maximum stress
θ_{mech}	Mechanical angle
τ_{max}	Maximum torque on the flexure

LIST OF ABBREVIATIONS

DAC	Digital to analog converter
DC	Direct current
DLP	Digital Light Projection
ESP32	Espressif system microcontroller
FEM	Finite element modelling
FR4	Flame retardant 4
GUI	Graphical user interface
LDV	Laser doppler vibrometer
MEMS	Electro-mechanical-systems
MOEMS	Micro-Opto-Mechanical systems
PCB	Printed circuit board
PDMS	Polydimethylsiloxane
PI	Polyimide
PID	Proportional–integral–derivative
PR	Piezoresistor
PSD	Position sensitive detector
PWM	Pulse width modulated
RMSE	Root mean squared error
TOSA	Total optical scan angle
1D	One-dimensional
2D	Two-dimensional
3D	Three-dimensional

1. INTRODUCTION

Today, the use of Electro-Mechanical-Systems (MEMS) technologies is becoming increasingly widespread and the need for the use of miniature electronic devices occupies a large place. MEMS developed over the years have been combined with optics, resulting in the birth of a new discipline called Micro-Opto-Mechanical Systems (MOEMS). In this way, with devices produced at micron scale, light can be manipulated and used in various ways. Within this discipline, low-cost, low-energy consumption, miniaturization, and portability are some of the important parameters [1] MEMS scanners. Therefore, with the development of new fabrication methods, cheaper and faster devices can be used in communication networks, medical devices, various display and imagining systems, optical lithography, spectroscopy, etc. In recent years, microscanner technologies have formed a very large part of the field of MOEMS. Applications where microscanner technologies provide various solutions can be specified as biomedical imaging devices [2–4], lidar systems [5, 6], imaging systems [7], projection displays [8–11], pico projectors [12], laser camera [13, 14], Digital Light Projection (DLP) [15], adaptive optics [16], fiber optic switches [17], spectrometers [18, 19], confocal microscopes [20, 21], and barcode readers [22, 23]. Some of these devices are shown in Figure 1.1.

Microscanners act as a thin moving mirror. Power consumed by microscanners, scan sizes, and scan patterns vary according to the systems they are used in [24]. Microscanners have various scanning types, including one-dimensional (1D) [5, 25], two-dimensional (2D) [26, 27], and three-dimensional (3D) ones [28]. They can reflect the desired image by scanning a certain surface area in line with their purpose. Uniaxial scanners scan a linear line on a single axis, and the point at which the scanned line has the greatest length gives us at what frequency the scanner achieves maximum displacement. However, microscanners need to reveal specific patterns on purpose. 2D microscanners have three different scanning methods. These are referred to as (1) Spiral scanning [29], (2) Lissajous scanning [30, 31], and (3) Raster Scanning [32] as shown in

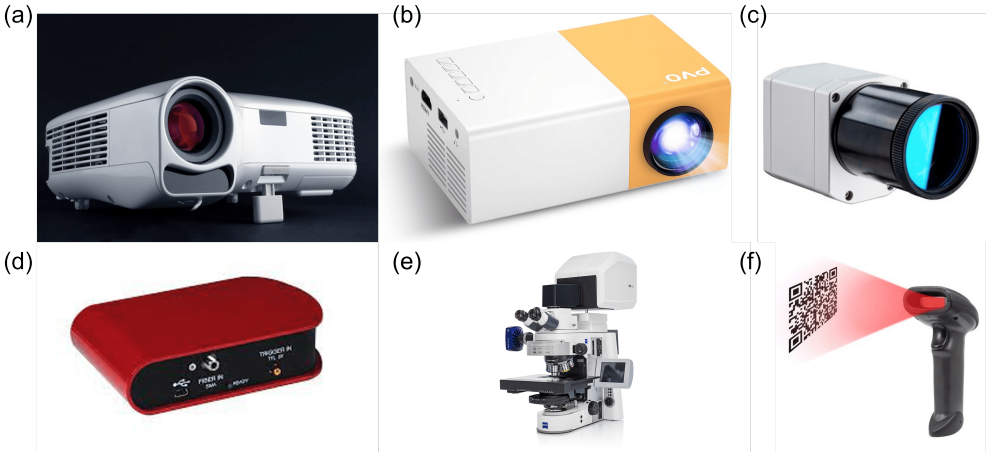

Figure 1.1: Various application examples of the optical MEMS technologies. (a) projection display, (b) pico projector (PVO ®Portable Projector), (c) laser camera (Optris®PI 08M), (d) spectrometer (Thorlabs®CCS100 Compact Spectrometer), (e) confocal microscopy (ZEISS®LSM 900), and (f) barcode reader (Adesso®NuScan 2500CU).

Figure 1.2. These methods have their differences with respect to each other, such as moving types. In the spiral scanning method, a circular form is created with sinusoidal and cosine waveforms created at the same frequency but with different amplitudes in the x and y orbits. In Lissajous scanning, waveforms are generated at different angular frequencies, and they overlap on both the x and y axes, creating various curves. In the raster scanning method, while the waveform is moving along the x-axis in the horizontal axis, it is ramped step by step on the y-axis. As a result, a triangular form occurs on the x-axis [33]. Moreover, microscanners need to reveal specific patterns on purpose. In order for a scanner to provide these patterns, certain mechanisms must be created to actuate the structure. There are various operating methods used for this purpose. These are (1) magnetic [34–38], (2) piezoelectric [39–42], (3) electrothermal [43–45], and (4) electrostatic actuations [46–49].

In scanners, low power consumption, high scanning angle, and low resonance frequency play critical roles [50]. For this reason, the substrate material of the scanner is one of the important parameters in order to have maximum displacement and scanning area under minimum external force. In the selection of the substrate material, its cost,

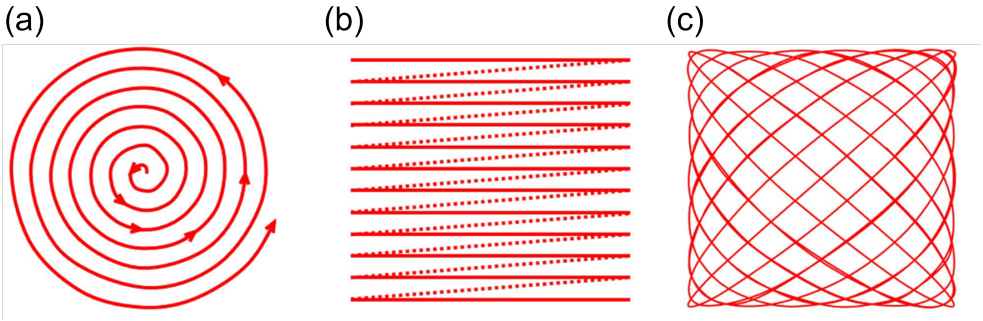

Figure 1.2: Examples of the scanning trajectories. (a) Spiral scanning, (b) Raster scanning, and (c) Lissajous scanning [29].

surface smoothness, and flexibility play a critical role. Various materials such as silicon [51], polydimethylsiloxane (PDMS) [52], Steel [53, 54], FR4 [18, 55, 56], and Polyimide (PI) [57] have been used as the main fabrication material for the microscanners.

Among the existing fabrication materials, polyimide material is chosen for its low-cost, ease of fabrication and having a low resonant frequency. The reason why it can work effectively at low frequency is that it has a low Young's modulus, and hence high flexibility, compared to materials such as FR4 and steel. Thus, it can exhibit similar displacement and scan angle amount at a lower frequency compared to other materials under the same design and same external force. Additionally, the polyimide material has high tensile strength and very high responsiveness to external stimuli, and therefore, it is considerably suitable in terms of preventing a deformation that may occur in the microscanner flexures against torsional movement.

These scanning systems are able to be controlled with open-loop and closed-loop [58–63] systems. Closed-loop control systems are a more preferred method as they can better maintain operational efficiency. The real-time detection of the scanning angle of the scanner is required for the closed-loop.

In open-loop control, factors such as temperature and pressure cause inaccuracies and deviations on the system. Therefore, a feedback control loop has been developed to detect these factors. This closed-loop system can be established by continuously calculating the error value with the proportional–integral–derivative (PID) controller. In

other control methods, system elements such as controller, non-linear switch, observer, and position sensitive detector (PSD) are used together for flatness-based control and sliding-mode control [58]. In another work, the angular position of the scanner is measured by placing a PSD on the surface where the laser is reflected. The feedback is adjusted to change the frequency of the system [59]. Additionally, the change in motion is able to be read over the Wheatstone bridge circuit by using a piezoresistive element to the bending points in order to detect the change in position. In this study, closed-loop can be achieved with PID control for the proposed method [60].

There are various sensing methods to measure the rotation angles and positions of scanners with various scanning types [64]. These methods are capacitive sensing method [65], piezoresistor-based method (PR) [66], magnetic internal sensing method [55,67,68], and optical feedback method [18,69,70]. The specified sensing methods differ according to the various actuation methods in use. The capacitive sensing method is used in scanners with electrostatic actuation method, where an interaction between the driving and the sensing signal is [65]. The piezoresistive sensing method is integrated into the torsion beams i.e. the flexures of the microscanners, and thus is used for a position sensing during the scanning angle made by the scanner [71]. The magnetic sensing method is used to sense the magnetism or electric effect created on the scanner. However, since it is difficult to separate the magnetic field lines in 2D scanners with this method, it is more suitable for 1D scanners [67]. Finally, the optical feedback method is used to sense the laser beam reflected from the scanner with a photodiode or a photodetector to obtain the position and angle information of the mirror [72–74].

In this study, an one-dimensional (1D) polyimide-based magneticly actuated microscanner is presented to be used in applications requiring wide aperture and low-frequency. In the presented study, polyimide material, which has high flexibility, as well as being cheap and easy to fabricate, is used. Since polyimide material has lower Young's Modulus and Torsional Modulus compared to steel and silicon, compared to other materials under the same physical properties, the scanner has a high scanning angle and creates a durable system with high displacement in the torsion beams [75].

The planar electrocoil is embedded on the microscanner and as a monolithic structure increases the effect of magnetic actuation.

For the feedback mechanism, electrically high resistance graphite paste (Bare Conductive ®Electric paint) is used due to its adhesion to the polyimide surface, fast-responded, easy and quick-to fabricate by means of a mask because there is no need for a clean room, low-cost and capable of highly sensing. Through the graphite material, a sensitive detection system is obtained, and it eliminates the requirements of complex mechanisms that require high energy consumption.

The rest of this paper is organized as follows: In Chapter 2, operation principle of the proposed system is explained. Subsequently, proposed design of the microscanner and its magnetic actuation mechanism are eloborated in Chapter 3 and 4, respectively. In chapter 5, electronic read-out circuitry is presented. The experimental test setup along with the calibration and test results are shown and demonstrated in Chapter 6. Finally, in Chapters 7 and 8, the novelties of this study, comparison of test results with the studies in the existing literature, and conclusions with numerical data are presented.

2. PROPOSED SYSTEM

The system that is proposed within this thesis, is illustrated in Figure 2.1. It is composed of five fundamental components. These are (1) a polyimide-based microscanner structure whose top surfaces of its flexures are coated with thin-film piezoresistive layers shown in Figure 2.1, (2) a feedback circuitry composed of a conventional voltage divider circuit to detect changes in resistance due to stress caused by flexure buckling on the piezoresistive graphite layers, (3) a generic espressif systems (ESP32-WROOM-32) generating a signal to drive the microscanner and to receive and process the feedback signal, (4) a power amplifier (TDA8932) to drive the planar electrocoil, and (5) 5 mW laser-source (RYS1230) with 650nm wavelength along with its custom-made switching circuitry. The novelty of the polyimide-based 1D scanning microscanner system in this work lies in piezoresistive feedback-scanning interaction.

Proposed microscanner structure is designed and fabricated from a low-cost, and flexible polyimide material [76]. Anchor point of flexure is coated with a thin-film piezoresistive graphite layer (Bare Conductive®Electric paint) for detection. Additionally, copper layers that form the planar electrocoil are embedded onto microscanner and the conductive pads are used for electrical conduction so that current can be supplied to the electrocoil.

Polyimide-based microscanner is located at the core of this system as depicted in Figure 2.1. In this 1D microscanner system, the laser beam that is generated utilizing a 5 mW collimated laser source with 650nm wavelength is hit onto the inner frame of the microscanner and is reflected back from it. Thereby, the laser beam scans a planar line within the region where it is reflected. Scanning is performed by the 1D-movement of the microscanner as a single axis. Microscanner performing as 1D-movement is magnetically actuated. In order to increase the dynamic range of the scanning and maximize the delivered magnetic force, a planar electrocoil is embedded in the inner frame of the microscanner. Subsequently, a neodymium magnet is placed under the

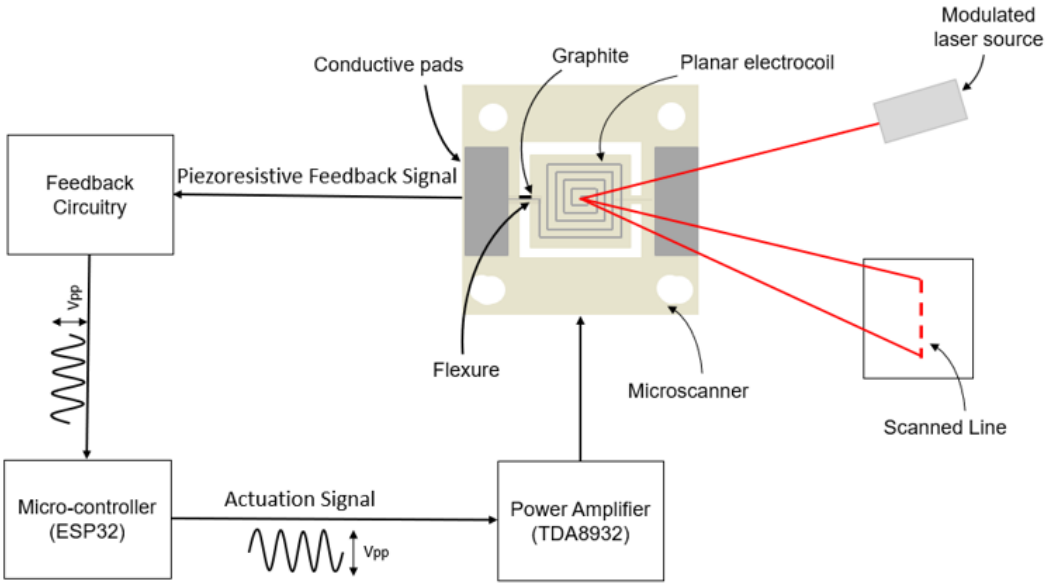

Figure 2.1: System diagram of the proposed polyimide-based microscanner system. The system harbors a generic ESP32 microcontroller (ESP32-WROOM-32), a power amplifier (TDA8932), a feedback circuitry system, a 5 mW laser-source (RYS1230) with 650nm wavelength along with its custom-made switching circuitry, and finally a polyimide-based microscanner together with conductive pads and planar electrocoil.

cage plate (Thorlabs02/M-SM1) that is used to immobilize the microscanner structure. Thus, the magnitude of the magnetization vector H-field stemming from electrocoil is saturated, and the displacement of the microscanner movement is further increased.

The driving signal required for the 1D-mechanical movement of the microscanner is formed using a generic ESP32 microcontroller. Since the generated driving signal is not sufficient for the planar electrocoil to provide the magnetic field required to operate the scanner, a power amplifier (TDA8932) is used to increase the signal. Connection of the generated signal and the electrocoil is provided by the conductive pads on the microscanner that is connected to the electrocoil by thin copper layers passing over the flexures. In addition, the frequency given to the system is gradually increased via the ESP32 microcontroller with the 1 Hz step size in order to accurately determine the resonance frequency range of the microscanner.

In order to have an auto-tune property and to consistently lock to the resonant

frequency, a feedback mechanism is constituted. For this feedback mechanism, the piezoresistive sensing method is preferred due to its low-cost, fast-responded, easy and quick-to-fabricate, and sufficiently sensitive graphite paste is used. Graphite is coated on the anchor of microscanner torsional beam where the stress intensity is high.

The scanning motion increases gradually until it reaches the resonant frequency at which it performs the highest scanning angle [6,35]. In the meantime, the flexure of the microscanner, which is coated with graphite, is exposed to torsion. Therefore, tensile stress is occurred due to torsion, and the geometry of the piezoresistive graphite layer changes, and hence resistance change. The formula describing this relationship between the piezoresistive geometry and the resistance change (ΔR) is given in Equation 2.1 from [77].

$$R_{PR} = \rho_{PR} \frac{L_{PR}}{A_{PR}} \tag{2.1}$$

where ρ_{PR}, L_{PR}, and A_{PR} correspond to resistivity of the piezoresistive material, length of the piezoresistive layer, and cross-section of the piezoresistive layer, respectively. Depending on the deformation stemming from the torsional movement of the flexure, a resistance change (ΔR) at the anchor point is occurring. Resistance change is collected and transformed into a voltage signal, which is a feedback signal, with a voltage divider circuit. Subsequently, the collected feedback signal is transmitted to the ESP32 microcontroller. This microcontoller produces also the driving signal required for the actuation of the microscanner. Thus, the amplitude of the feedback signal coming from the graphite via the voltage divider and indirectly the microscanner is captured and detected by the ESP32. Therefore, the resonance frequency at which the maximum scanning angle of the microscanner and hence the maximum torsion in the flexures occurs is determined.

However, when the polyimide-based microscanner actuates and the current given to the copper planar electrocoil embedded in it, the structure increasingly becomes warmer and the flexibility of the material increases, and then the spring softening effect is observed. As a result, the change in the resonant frequency of the scanner occurs. It is important to monitor this change in order to maintain the operating efficiency of the system. The resonance frequency must be adjusted momentarily in order for the scanner to remain stable at the maximum scanning angle, that is, in the resonance mode. For this purpose, a piezoresistive feedback system has been added as mentioned above. The frequency shift stemming from the spring softening effect is monitored momentarily and the resonant mode is maintained by the self-tuning of the system.

3. MICROSCANNER DESIGN

In this chapter, details of the microscanner design are explained. Section 3.1 elaborates the proposed microscanner structure, FEM analysis, and its design parameters and related dimensions.

3.1. Microscanner Structure

The design parameters are directly effective on the overall performance of the polyimide-based microscanner structure and play a vital role to develop and acquiring a more sensitive structure. Some constraints are required to optimize the scanner structure. In this work, these constraints are tabulated in Table 3.4. These constraints express the length (L_{of}) and width (w_{of}) of the outer frame of the scanner structure, diameter of the mounting hole (w_o), width of the planar electrocoil copper line (w_{cl}), distance between two copper lines of planar electrocoil (w_p), thickness of the scanner structure (t_s), and the maximum aperture ($L_g \times w_g$) related with the scanner geometry, respectively.

The first two constraints are related to the optomechanical component used to fix the scanner. The values of the length L_{of} and width w_{of} of the outer frame are chosen as approximately 40 mm, and diameter of the mounting hole w_o is selected as approximately equal to the 6 mm, because of the 40 mm $\times$ 40 mm cage plate (Thorlabs®CP02/M-SM1) used to immobilize the scanner structure, and M4 mount-

Table 3.1: Constraints of our proposed polyimide-based microscanner structure.

	Design Constraints
(1)	L_{of} and $w_{of} \simeq 40\ mm$
(2)	$w_o \simeq 6\ mm$
(3)	w_{cl} and $w_p \geq 60\mu$m
(4)	$t_s \geq 80\mu$m
(5)	$L_g \simeq 17\ mm$ and $w_g \simeq 16\ mm$ (max aperture for inner frame)

ing hole that is located onto the cage plate.

The third constraint is associated with the planar electrocoil. The geometry of the planar electrocoil is important in order to be able to create an effective magnetic field which provides the scanner to start moving. As detailed in Chapter 4, the geometry of the planar electrocoil, its inductance, number of turns, and material properties has considerable importance on the magnetic flux and magnetic field.

For these reasons, according to the minimum fabrication limits of PCBWay company for the copper line, the width of the planar electrocoil copper line w_{cl} and the distance between the two copper lines in the planar electrocoil w_p are chosen as 60μm, and also, since the fourth constraint, the scanner thickness t_s, is opted as 116μm, the planar electrocoil thickness t_c is 35μm.

The final constraint, the maximum aperture size, plays a critical role in determining the scanner geometry. In order to create a monolithic system, the Wheatstone circuit with an amplifier, which is a read-out circuit for future use, is designed to occupy a minimum space and placed on the outer frame of the structure. The surface area occupied by the circuit on the outer frame is 24 $mm \times 12\ mm$. As a result of this, maximum aperture size is able to be 17 $mm \times 16\ mm$ ($L_g \times w_g$) where the scanner will be placed.

There are some important parameters for microscanner design within the framework of this determined area. These are (1) having low resonance frequency, (2) having high displacement under low resonance frequency, and hence high mechanical scanning angle, and high stress amount, and (3) having maximum number of turns of the integrated planar electrocoil for magnetic actuation. In order to determine the design parameters for both the microscanner and the flexures, the following formulations are used and various FEM analyzes are performed [75].

Equation 3.1 expresses the resonant frequency (ω=$2\pi f$) and the parameters it de-

pends on for the rectangular scanner in torsional mode. In the equation, K_s represents the spring constant, while I_m in represents the inertia of the microscanner [75].

$$\omega = \sqrt{\frac{K_s}{I_m}} = \sqrt{\frac{24K_{ab}Gab^3}{L_f \rho t_s L_s {w_s}^3}} \tag{3.1}$$

$$\begin{aligned} K_s &= \frac{2I_p G}{L_f} \\ I_p &= K_{ab} a b^3 \\ K_{ab} &= (5.33 - 3.36\frac{b}{a}(1 - \frac{b^4}{12a^4})) \end{aligned} \tag{3.2}$$

K_s is shown in Equation 3.2 and it is about the torsional flexure beam. In the Equation 3.2, I_p represents the flexure polar moment of inertia. G and L_f symbolise torsional modulus and length of the flexure beam. I_p depends on the constant K_{ab} and the parameters a and b, which are half the width of the flexure ($w_f/2$) and half the thickness ($t_s/2$) [75]. b parameter is 65μm and fixed due to the thickness of the microscanner structure is determined as 130μm. According to the equation, parameter C is directly affected depending on the size of the flexure beam width (w_f). However, the flexure width (w_f) should be as minimum as possible, as the extension of the flexure beam width is resulted in an increase in the spring constant (K_s) and hence the resonant frequency (ω=2πf). The result of the eigenfrequency analysis showing the effect of various flexure beam widths (w_f) on the resonance frequency is indicated in Figure 3.1. As a result of the simulation, it is seen that the resonance frequency increases from 123Hz to 252Hz as the flexure beam width increases from 0.2 mm to 0.8 mm for 10 mm $\times$ 10 mm inner frame. Based on constraint 2 and simulation results shown in Figure 3.1, the minimum possible width of the flexure beam (w_f) is determined as 200μm. L_f, which express the length of the flexure has a direct effect on

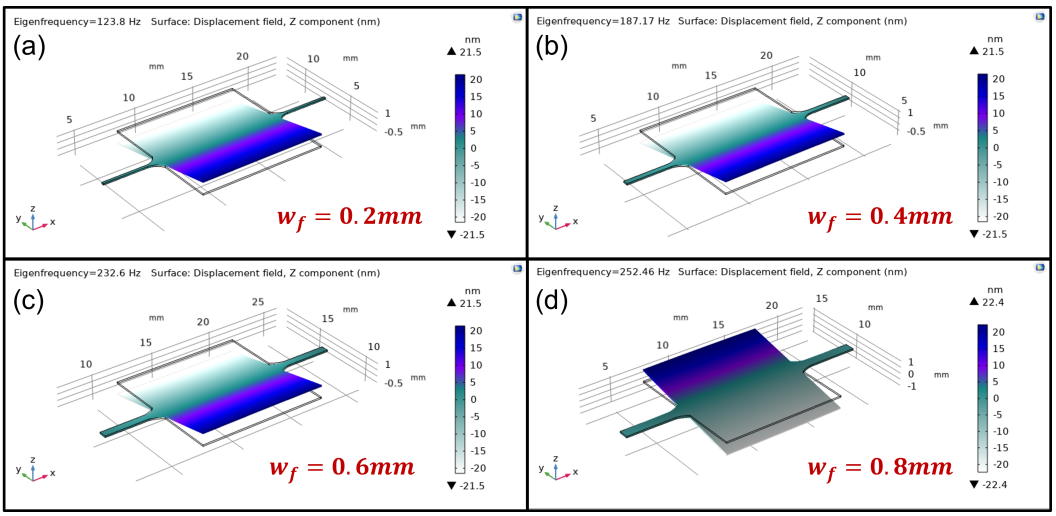

Figure 3.1: Eigenfrequency analysis results of the proposed polyimide-based microscanner in various flexure beam width (w_f).

the spring constant (K_s). The high length L_f is another critical parameter in reducing the spring constant (K_s), but since it negatively affects the amount of stress on the flexure beam shown in Equation 3.5, the length of the flexure beam (L_f) is determined according to the dimensions of the microscanner structure.

$$I_m = \frac{1}{12}\rho t_s L_s {w_s}^3 \tag{3.3}$$

$$\delta_{max} = 0.217\frac{\rho f^2 {w_s}^5 \theta_{mech}}{E{t_s}^2} \tag{3.4}$$

$$\tau_{max} = \frac{3K_{ab}Gb\theta_{mech}}{8L_f}[1 + 0.6095\frac{b}{a} + 0.8865(\frac{b}{a})^2 - 1.8023(\frac{b}{a})^3 + 0.91(\frac{b}{a})^4] \tag{3.5}$$

Table 3.2: Theoretical calculation of the proposed microscanner in torsional mode.

Scanner Inertia	**Spring Constant, Flexure polar moment of inertia**	**Resonant Frequency (Hz)**
$\mathrm{I}_m = \frac{1}{12}\rho t_s L_s {w_s}^3$	$\mathrm{K}_s = \frac{2I_pG}{L_f}$ $\mathrm{I}_p = K_{ab}ab^3$ $\mathrm{K}_{ab} = (5.33{-}3.36\frac{b}{a}(1{-}\frac{b^4}{12a^4}))$	$\mathrm{f}_r = \frac{1}{2\pi}\sqrt{\frac{K_s}{I_m}} = \sqrt{\frac{24K_{ab}Gab^3}{L_f\rho t_s L_s {w_s}^3}}$
$\mathrm{I}_m = 1.1883E-09$	$\mathrm{K}_s = 3.0655E-04$ $\mathrm{I}_p = 6.5971E-17$ $\mathrm{K}_{ab} = 3.3812$	$\mathrm{f}_r = \frac{1}{2\pi}\sqrt{\frac{K_s}{I_m}} \simeq 86.52$

I_m is shown in Equation 3.3 and it is about the microscanner in rectangular form. In the Equation 3.3, ρ represents the density of the material used tabulated in Table 3.3. t_s is the thickness of the scanner structure and is chosen as 116μm as stated above. L_s and w_s express the length and width microscanner structure. As can be seen in the Equation 3.3, an increase in inertia occurs when the length (L_s) and width (w_s) of the microscanner increase. The inertia behaves inversely with the resonant frequency and causes a decrease in the frequency amount. Within the scope of the above-mentioned design parameters, the dimensions of the scanner structure should be as high as possible in order to obtain a high number of turns of the planar electrocoil and a system with a lowest resonance frequency. Additionally, the very low difference between the length (L_s) and width (w_s) of the microscanner structure is significant for dynamic deformation, as can be understood from Equation 3.4 [75]. The theoretical result of the polyimide-based microscanner is tabulated in Table 3.2.

The result of the eigenfrequency analysis showing the effect of various flexure beam lengths (L_f) on the resonance frequency is indicated in Figure 3.2. According to the simulation result, as a result of reducing the length of the flexure beam length (L_f) up to a certain point, there is a direct proportional decrease in the resonance frequency. If the flexure beam length (L_f) is between 1.5 mm and 2 mm, the lowest resonance frequency is obtained. In this way, 1 mm gaps are left within the scope of the aperture size so that the movement of the microscanner is not restricted, and the length of the microscanner (L_s) is determined as 15 mm and the width (w_s) as 14 mm. Therefore,

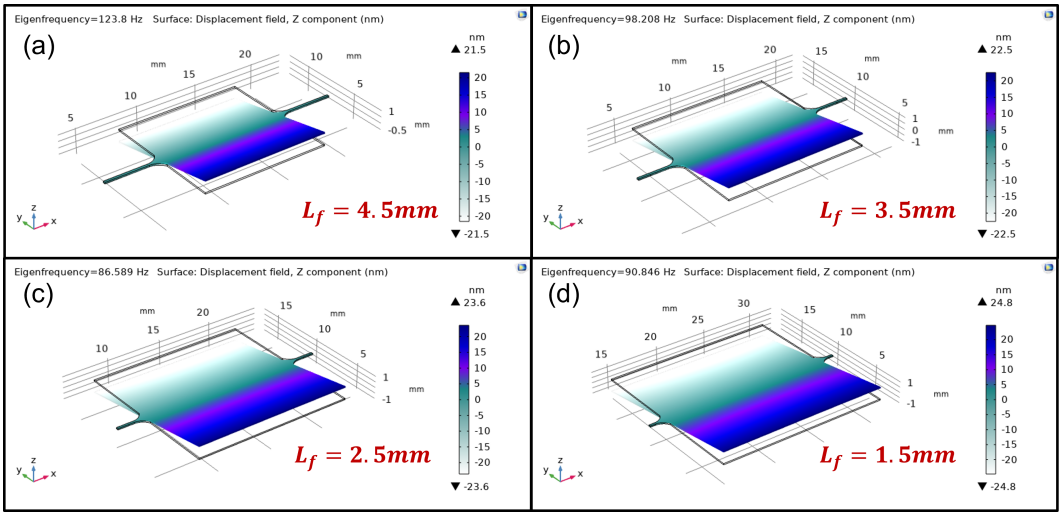

Figure 3.2: Eigenfrequency analysis results of the proposed polyimide-based microscanner in various flexure beam length (L_f).

Table 3.3: Properties of Polyimide and copper used as composite in mechanical design.

Parameters	**Values**
Composite Torsional Modulus (GPa)	5.067
Composite Poisson's Ratio	0.34
Composite Density (Kg/m^3)	2842

the length of the flexure beam length (L_f) is chosen as 2 mm. The properties that make up the main material of the microscanner and are used as material parameters in the simulation are summarized in Table 3.3.

A three-dimensional (3D) technical drawing of the polyimide-based 1D microscanner along with its dimension parameters is depicted in Figure 3.3. The design parameters which are directly effective on the overall performance of the polyimide-based microscanner structure, are tabulated in Table 3.4. As shown in figure 3.3, the values of the length L_{of} and width w_{of} of the outer frame are both approximately 40 mm because of the 40 mm $\times$ 40 mm cage plate (Thorlabs®CP02/M-SM1) used to immobilize the scanner structure.

L_s symbolizes the length of the microscanner (inner frame) whereas w_s illustrates the width of it. L_{cp} and w_{cp} define the length and width of the one conductive pad,

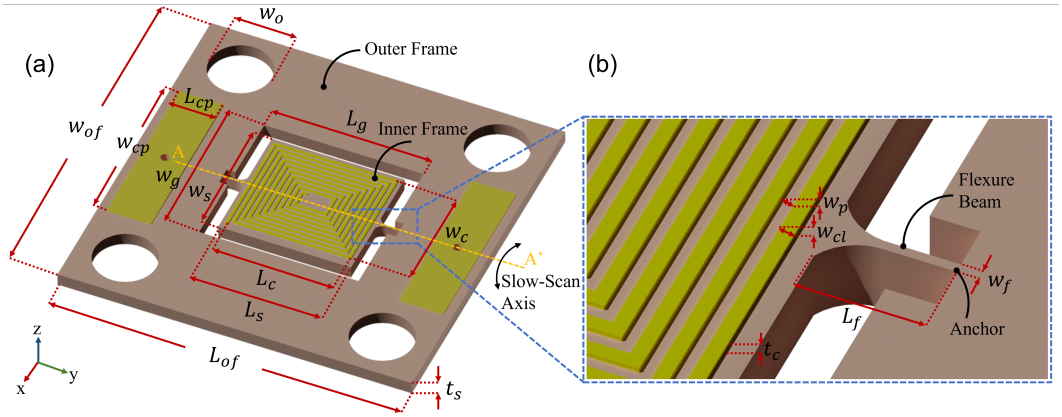

Figure 3.3: (a) Technical drawing of the proposed generic 1D polyimide-based microscanner and its design parameters, (b) a close-up view of the flexure beam.

respectively. Additionally, L_c indicates the length of the planar electrocoil structure that is located onto the microscanner, whereas w_c represents the width of it. They are equal 14.88 mm and 13.88 mm, respectively because of the 60μm gap from the both sides. Finally, t_s expresses thickness of the microscanner structure which is selected as 116 μm. The value of w_o width of holder holes is chosen as approximately equal to the 6 mm because of M4 mounting hole that is located onto the cage plate, and L_g indicates the length of the innerframe opening and its maximum value can be 17 mm according to the maximum aperture.

Figure 3.3b illustrates the close up view of the flexure of the proposed microscanner. L_f and w_f indicate the related length and width of the flexure beams, respectively. Moreover, w_{cl} states the width of the planar electrocoil line, and w_g expresses the gap between two planar electrocoil lines. Their values are approximately 60 μm because of the minimum fabrication limit. Planar electrocoil, as shown in Figure 3.3 is opted over a complete area on the microscanner in order to be able to enable the movement of the microscanner which is triggered with an external magnet. The microscanner makes a resonant torsional movement onto A-A' axis as indicated in the Figure 3.3.

Figure 3.4 shows the results of eigenfrequency analysis at various modes for the proposed polyimide-based scanner design to understand the resonant frequency of the scanner used in subsequent experiments in different modes. Resonant modes of the

Table 3.4: Parameters and related values of the proposed system indicated in Figures 3.3.

Parameters	**Descriptions**	**Designed (mm)**
L_{of}	Length of the outer frame	40
w_{of}	Width of the outer frame	40
L_{cp}	Length of the copper conductive pad	6.0
w_{cp}	Width of the copper conductive pad	18
w_o	Diameter of screw hole	6.0
L_s	Length of inner frame	15
w_s	Width of inner frame	14
L_c	Length of planar electrocoil	14.88
w_c	Width of planar electrocoil	13.88
L_g	Length of the outer frame aperture	17
w_g	Width of the outer frame aperture	16
t_s	Thickness of the scanner	0.116
w_{cl}	Width of the planar electrocoil copper line	0.06
t_c	Thickness of the copper line	0.5
w_p	Distance between two copper lines of planar electrocoil	0.06
L_f	Length of the flexure beam	2.0
w_f	Width of the flexure beam	0.2

proposed scanner according to the simulation results given in Figure 3.4 are tabulated in Table 3.5.

In consequence of the simulation, the resonance frequencies according to the 1D movements and the displacement values in terms of the obtained resonance frequencies are detected. As it can be seen from obtained values, torsional mode (Mode 1) of the proposed scanner is occurring at 81.626 Hz, as seen in Figure 3.5a and the stress at the anchor points in torsional mode is determined as 480 Pa, as given in Figure 3.5b. Here, it is important to note that maximizing the total-optical-scan-angle (TOSA) values of these modes using a limited power budget and cheap actuation components is the main aim of this work. A depiction of the fabricated polyimide-based microscanner is given in Figure 3.6a, close up views of the graphite coated flexure beam and conductive pad,

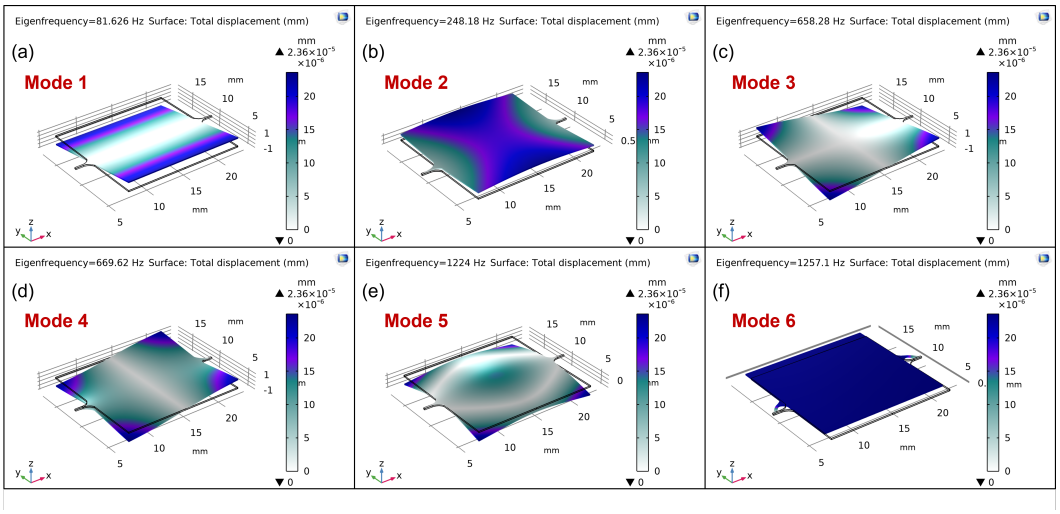

Figure 3.4: Eigenfrequency analysis results of the proposed polyimide-based microscanner in various eigenfrequency values.

Table 3.5: Resonance frequency values of first six modes of proposed scanner.

Scan Mode	**Scan Mode Resonance Frequency (Hz)**
Mode 1	81.626
Mode 2	248.18
Mode 3	658.28
Mode 4	669.62
Mode 5	1224
Mode 6	1257.1

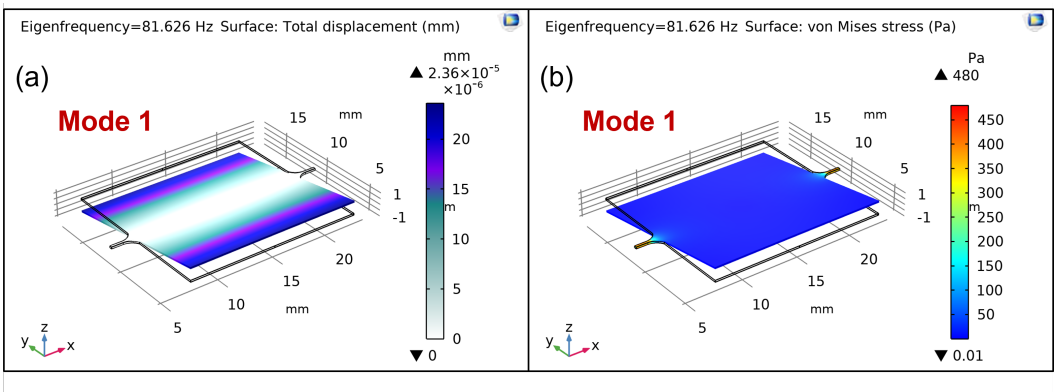

Figure 3.5: Eigenfrequency analysis and finite element method (FEM) results of the proposed polyimide-based microscanner (a) targeted slow-scan moded of inner mirror torsion mode at 81.626 Hz and (b) stress analysis at the anchor points (σ_{max}=480Pa).

back side of the flexure beam, and planar electrocoil shown in Figure 3.6b, c, and d, respectively.

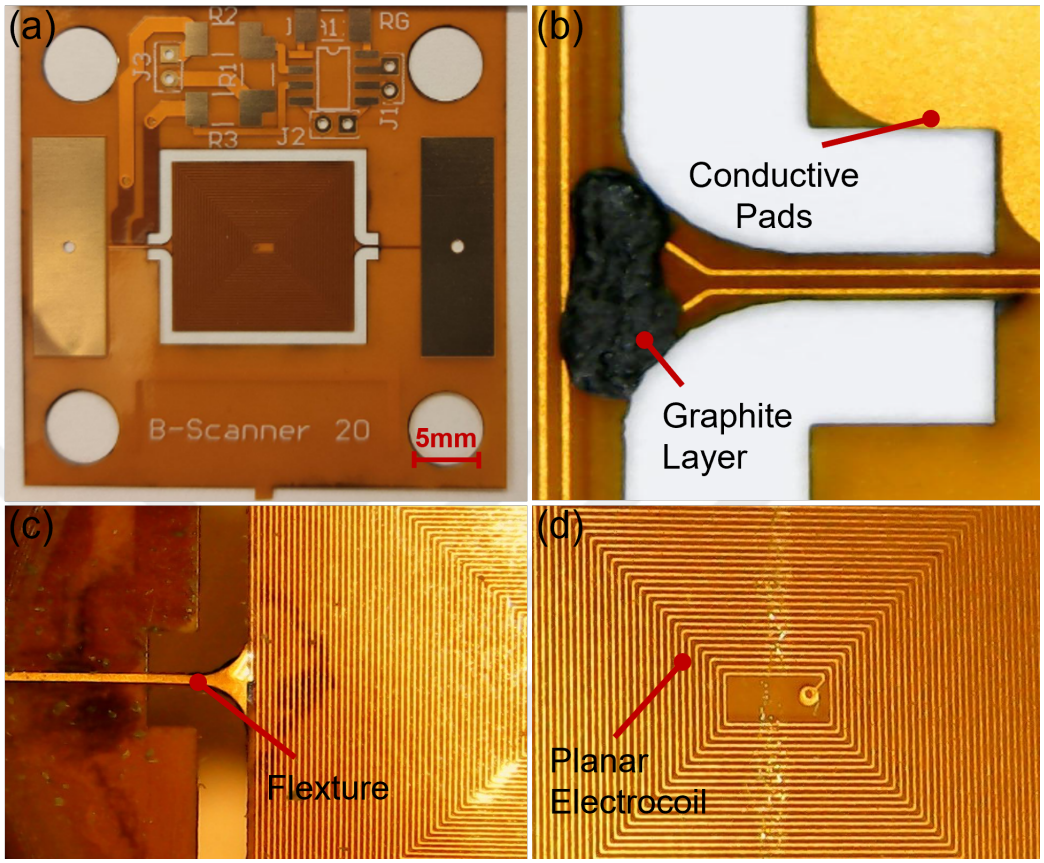

Figure 3.6: (a)View of the fabricated polyimide-based microscanner along with the scale bar, (b) close up view of the graphite coated flexure beam along with embedded wire connections, and conductive pad, (c) close up view of the flexure beam back side, (d) close up view of planar electrocoil.

4. MAGNETIC ACTUATION

In this chapter, details of the magnetic actuation principle of the scanner is explained. In section 6.1, the basic magnetization and hysteresis behavior are elaborated. Section 6.2 presents the planar electrocoil design, optimization, and characterization. Finally, Section 6.3 summarizes the Lorentz force describing the relationship between the planar electrocoil and the external magnet.

4.1. Planar Electrocoil Design and Measurement

In this section, the design and characterization of the planar electrocoil used to generate the magnetic field is discussed. In this study, a planar electrocoil with rectangular geometry is preferred in order to use the available surface area effectively due to the rectangular geometry of the microscanner structure and to create a higher number of turn and hence magnetic field. The technical drawing of the proposed electrocoil is shown in Figure 4.1, while the design parameters are tabulated in Table 4.1.

In this table, N is the number of turn. L_c is represented as the length of planar electrocoil whereas w_c, w_{cl}, and w_p indicates the width of planar electrocoil, width of the planar electrocoil copper line, and distance between two copper lines of planar electrocoil, respectively. Additionally, d_{in} is symbolized the distance of the inner gap of planar electrocoil, and ρ_{wire} describes the resistivity of the copper that is opted to create spiral structure. Finally, μ_r and μ_0 are the relative permeability, and permeability of free space of the material, respectively.

The planar electrocoil geometry is considerably preferred because of its thermal resistance, an effective magnetic field, and allowing a flexible and monolithic system [57, 78, 79].

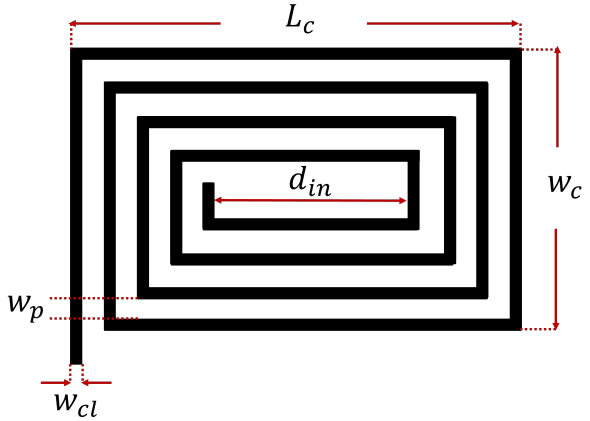

Figure 4.1: Technical drawing of the rectangular planar spiral electrocoil along with its design parameters.

Table 4.1: Parameters and related values of the proposed system indicated in Figures 4.1.

Parameters	**Descriptions**	**Values**
L_c	Length of planar electrocoil	14.88 mm
w_c	Width of planar electrocoil	13.88 mm
w_{cl}	Width of planar electrocoil copper line	0.06 mm
w_p	Distance between two copper lines of planar electrocoil	0.06 mm
d_{in}	Distance of the inner gap of planar electrocoil	1.44 mm
N	Number of turn	57
μ_r	Relative permeability	0.99
μ_0	Permeability of the free space of the material	$4\pi \times 10^{-7}$
ρ_{wire}	Resistivity of the copper	1.68×10^{-8} $\Omega.m$

Planar electrocoils consist of a closed loop, and therefore the input and output pins are designed to be located on two separate layers in order to provide the necessary current for the coil to operate [80]. Coil dimensions play a critical role in creating the desired effective magnetic field. The reduction in coil sizes causes the magnetic effect to decrease as shown in Equation 4.2, 4.6, and 4.7 [81, 82]. Therefore, the coil with the highest rectangular dimension and number of turns that can be made within the scope of the scanner constraints should be obtained. Increasing the number of turns,

N, is important to prevent ohmic losses and damage stemming from overheating [83, 84].Therefore, The electrocoil induction can be calculated with the following formula 4.1:

$$L_{rectangle} = \frac{N^2 \mu_0 \mu_r A}{I} \tag{4.1}$$

where, $L_{rectangle}$ expresses the inductance in henries (H), μ_r is the relative permeability of the core material in henries/meter (H/m), μ_0 represents the permeability of the free space of the material, N is the number of turns of wire in the coil, A is the area of the coil in square meters (m^2), I is the length of the coil in meters (m).

4.1.1. Magnetic Field of Rectangular Planar Electrocoil

The use of rectangular planar coils is preferred in the system. Inductance comparisons of various coil types are measured in the related article [85, 86]. As these measurements show, using planar coils is more advantageous in terms of sensing [87]. In addition to the high sensitivity of the planar coil, the fact that the coil is embedded on the scanner makes the system more compact. In many previous studies, it is seen that the coil is used as embedded because of its advantages [57].

One of these advantages is low-cost fabrication. The moving planar coil embedded in the polyimide-based microscanner has both more precision and low-cost since it does not require post-processing as it is realized during PCB fabrication process. For this reason, it is a more suitable option to provide the scanner and the coil in one piece. Additionally, the moving coil actuation has less inertia than the moving magnet actuation method, and the torsional bending of the flexure can be designed more compatible.

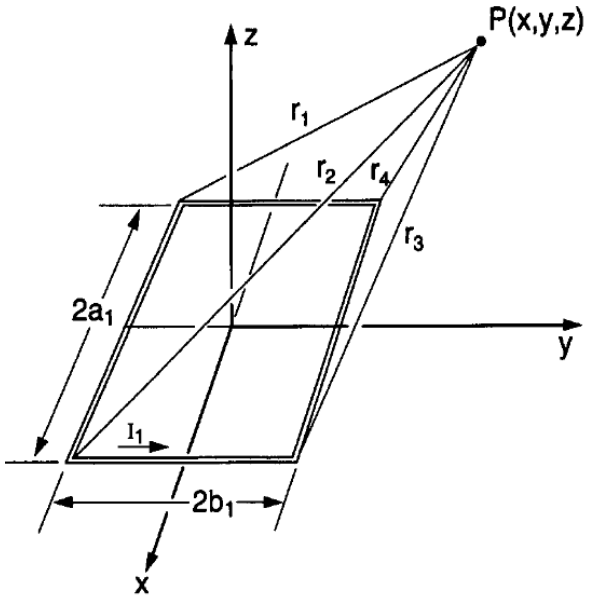

Figure 4.2: The geometry of the single turn rectangular planar coil. The magnetic flux density is evaluated at point P(x,y,z) [88].

The coil used in the system is positioned on the inner frame, which is the moving part of the scanner. A magnetic field is created by applying electric current to the coil through copper pads. Due to Ampere's law, a circular magnetic field is formed around the coil. Since a magnetic field will be formed on each wire turn, the number of turns and the magnitude of the magnetic field increase in direct proportion.

The magnetic field created by the coil is increased by a permanent magnet placed under the coil. Thus, both high power supply to the system and overheating are prevented. Thus, a magnetic field is created by the effect of the attractive and repulsive force between the electrically charged planar electrocoil and the permanent magnet. Thus, the movement of the flexible polyimide-based scanner with embedded coil is enabled. The magnetic field of the rectangular planar electro coil is shown in Figure 4.2 together with the magnetic flux density point (x,y,z).

The z-component of the magnetic flux density at P(x,y,z) is calculated with the Equation 4.2 [88]. In this Equation [88], C_a represents the sum of half the length of the planar electrocoil (L_c) and the distance from the current point to the x-axis. d_a expresses the sum of half the width of the planar electrocoil (w_c) and the distance from

the current point to the y-axis. Finally, r_a gives the equations of the distance of a point on the planar electrocoil to any selected P(x,y,z) point.

$$B_z = \frac{\mu_0 N I}{4\pi} \sum_{a=1}^{4} \frac{(-1)^a d_a}{r_a[r_a + (-1)^{a+1} C_a]} - \frac{C_a}{r_a[r_a + d_a]} \tag{4.2}$$

Where, C_a is given by

$$\begin{aligned} C_1 &= -C_4 = a_1 + x \\ C_2 &= -C_3 = a_1 - x \end{aligned} \tag{4.3}$$

Where, d_a is given by

$$\begin{aligned} d_1 &= d_2 = y + b_1 \\ d_3 &= d_4 = y - b_1 \end{aligned} \tag{4.4}$$

The distances r_1, r_2, r_3, and r_4 to the point P(x,y,z)where the magnetic flux density will be evaluated is calculated with the following Equations 4.5:

$$
\begin{aligned}
r_1 &= \sqrt{(a_1 + x)^2 + (y + b_1)^2 + z^2} \\
r_2 &= \sqrt{(a_1 - x)^2 + (y + b_1)^2 + z^2} \\
r_3 &= \sqrt{(a_1 - x)^2 + (y - b_1)^2 + z^2} \\
r_4 &= \sqrt{(a_1 + x)^2 + (y - b_1)^2 + z^2}
\end{aligned}
\tag{4.5}
$$

The magnetic flux density at the point P(x,y,z) in according with the x-axis shown in Equation 4.6, and y-axis shown in Equation 4.7 is given by

$$
B_x = \frac{\mu_0 N I}{4\pi} \sum_{a=1}^{4} \frac{(-1)^a z}{r_a [r_a + d_a]} \tag{4.6}
$$

$$
B_y = \frac{\mu_0 N I}{4\pi} \sum_{a=1}^{4} \frac{(-1)^a z}{r_a [r_a + (-1)^{a+1} C_a]} \tag{4.7}
$$

The planar electrocoil is designed considering the dimensions of the polyimide-based microscanner (15 mm×14 mm) whose design and width and proximity fabrication limit of the copper lines (60μm) is given in Table 3.4. In the design process, it is aimed that the coil has the highest magnetic field producing. For this purpose, the proposed planar electrocoil is designed with the lowest possible copper line width and proximity, as well as the highest number of turns. Design parameters and material properties are tabulated in Table 4.1. The magnetic field of the proposed electrocoil is monitored by increasing the distance along the x, y, and z axes for the excitation power at which the scanner resonates. These measurements are made by means of Gaussmeter (Alphalab®GM2) and the test setup is shown in Figure 4.3. The exper-

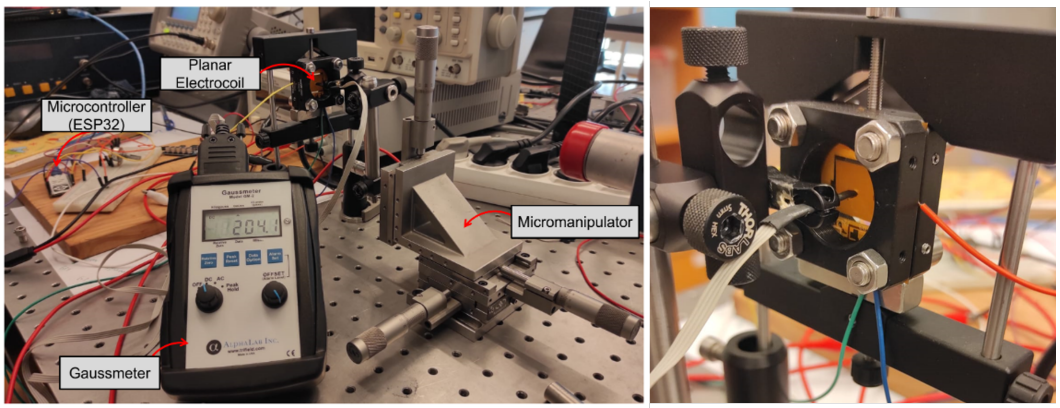

Figure 4.3: View of the measurement setup used to monitor the magnitude of magnetix flux created by proposed rectangular planar electrocoil at different axial and radial distances. The setup harbors three fundamental components: (1) Alphalab®GM2 Gaussmeter, (2) a generic ESP32 microcontroller (ESP32-WROOM-32), and (3) a Thorlabs®3D manual micromanipulator.

iment is carried out by connecting the measuring probe at the tip of the gaussmeter to the 3D micromanupilator and then moving it in the x, y (radial directions), and z (axial directions) axes, with a 200μm step size in the positive and negative directions, assuming the center point of the planar electrocoil. The test results obtained for each axis are reported in Figures 4.4, 4.5, and 4.6, respectively. As expected, the magnetic field magnitude of the electrocoil tends to decrease as it moves away from the axis, and decreases from there by almost a quarter at a distance of 10 mm from the initial position.

The behavior of magnetic flux density under radial distances is shown in Figure 4.6. The magnetic flux density is observed over a distance of 12 mm. While performing this measurement, as mentioned above, the axial distance is placed as zero by accepting the midpoint of the planar electrocoil of the measuring probe of the gaussmeter as the starting point. As expected, the magnetic field magnitude increases within the magnetic field directions from the midpoint of the planar electrocoil towards the negative z-direction.

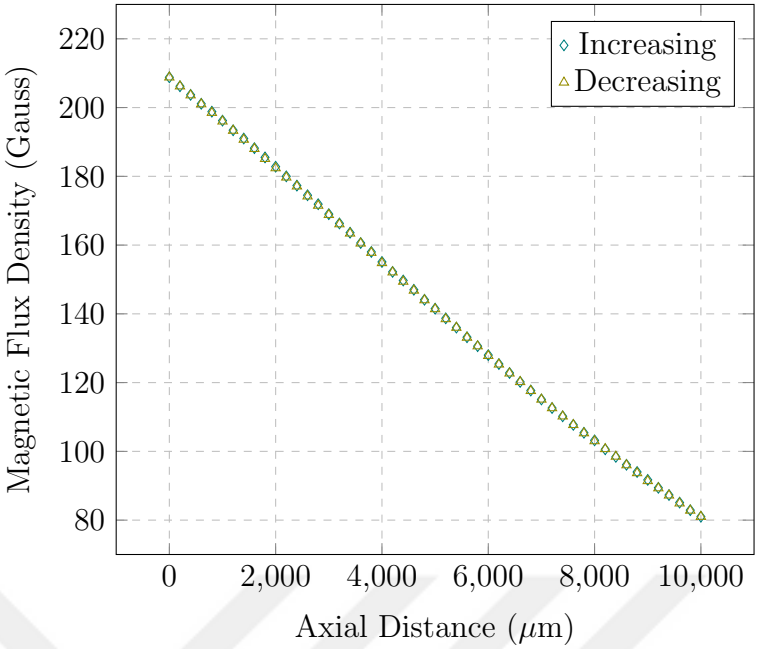

Figure 4.4: Magnetic flux density at axial distance in the x-direction.

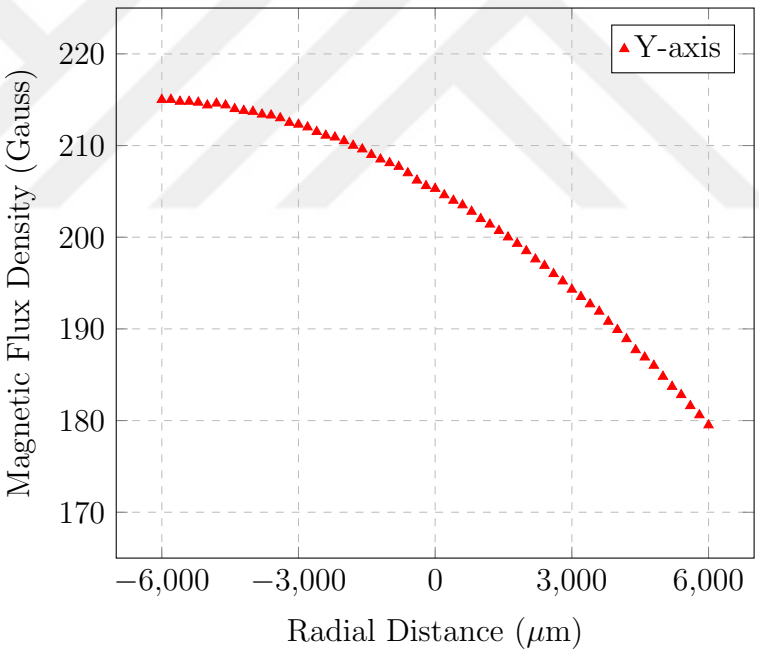

Figure 4.5: Magnetic flux density at axial distance in the y-direction.

4.2. Magnetic Coil Actuation: Lorentz Force

The magnetic field formed on the planar coil and therefore on the polyimide scanner is supported by adding a neodymium magnet. The magnet is placed as close to the polyimide scanner as possible and fixed on the setup. In the system, there

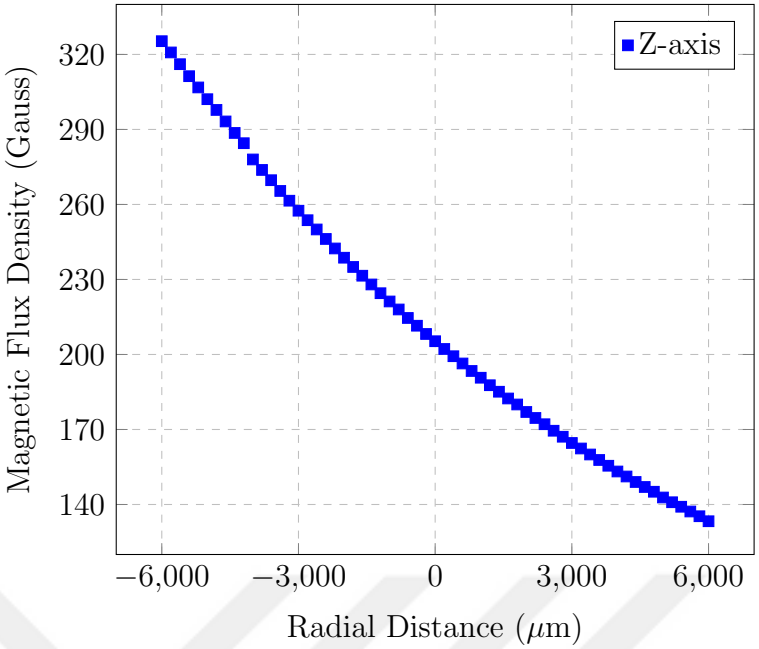

Figure 4.6: Magnetic flux density at radial distance in the z-direction.

is the electric field created by the electrocoil and the magnetic field created by the magnet. As a result of this interaction, the scanner moves and vibrates with the effect of the electromagnetic field. This force that the scanner is exposed to is called electromagnetic force or Lorentz force. The formula for the Lorentz Force are given the following Equations 4.8 [89].

$$\begin{aligned} F_E &= qE \\ F_B &= q(\vec{v} \times \vec{B}) \\ F_L &= F_E + F_B \\ F_L &= qE + qv \times \vec{B} \end{aligned} \tag{4.8}$$

In these equations, F_E represents the force stemming from the electric field. F_B indicates the force arising form magnetic field whereas q, v, and $\vec{B}$ express the charge on planar coil, velocity of charge, and magnetic field, respectively. Moreover, F_L sym-

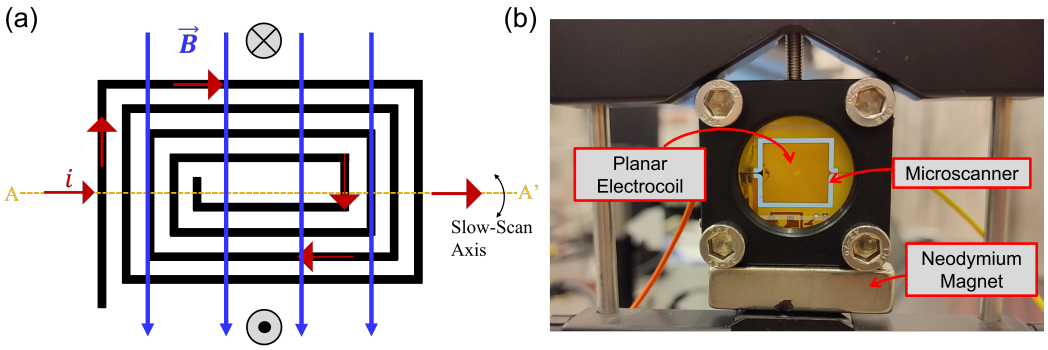

Figure 4.7: (a) Conceptual drawing of the direction of the magnetic field generated over the planar electrocoil. (b) position of the Neodymium magnet that has 20.5 mm width and 6 mm^2 cross-section, and electrocoil relative to the polyimide-based microscanner.

bolizes the Lorentz force that is sum of the F_E and F_B. The charge loaded (q_{load}) microscanner moves in the electric field with v velocity, and is exposed to magnetic field force $\vec{B}$. When the electrocoil carrying electric current stays in the magnetic field caused by the magnet in the system, the charges are exposed to the Lorentz force and create small cyclic forces on the wire. This force is called the Laplace force. Its relationship with electric current and Lorentz force can be seen in the Equation 4.9.

$$F = Il \times \vec{B} \tag{4.9}$$

Since the copper wire is a curved as a planar coil shape, the force on the wire is applied on every part of the wire. This force is calculated by integration with the Equation 4.10 shown below.

$$F = I \int dl \times \vec{B} \tag{4.10}$$

Copper wires heat up at the same time as current flows through them, but this heat is not examined in the article. The softening effect caused by the heated coil is explained in the Test Result section. The conceptual drawing of the direction of the magnetic field generated on the planar electrocoil and the position of the neodymium magnet are shown in Figure 4.7.

5. ELECTRONICS

The electronic system diagram is depicted in Figure 5.2. As mentioned above, the actuation is enabled by the magnetic field generated by the electrocoil on the microscanner. The electrocoil is actuated by means of a Espressif System Microcontroller (ESP32), which involves digital to analog converter (DAC). Primarily, it provides digital signal generation so that slow-scanning is able to be executed, then the generated digital signal is converted to analog signal. Subsequently, the signal generated from the ESP32, whose formula is given in Equation 5.1 below, is sent through the planar electrocoil via one of the DAC channels (GPIO25 & GPIO26) of ESP32 micro-controller. This transmission is carried out thanks to the conductive pads on the microscanner, to which the GPIO25 pin of the ESP32 is directly connected. Additionally, the output voltage of the ESP32 is 3.3V. The required frequency for the slow-scan is given by microcontroller. The sinosoidal signal generated from the microcontroller is shown in Figure 5.1 and microscanner resonates at 82 Hz.

$$t = i/f_s, sig[i] = (128.0 + 2.0 * (sin(2 * f * PI * t))) \tag{5.1}$$

The signal used to drive the electrocoil needs to be amplified in order for the scanner to be able to scan successfully in the desired range. For this purpose, TDA8932 class-D type power amplifier used as current amplifier shown in Figure 5.3 is used to amplify the actuation signal. The TDA8932 is an audio power amplifier using class-D technology, consisting of either a mono full-bridge or a stereo half-bridge. In the scope of working principle of TDA8932, the audio input signal is converted into a Pulse Width Modulated (PWM) signal via an analog input stage and PWM modulator. The continuous time output power is 2 $\times$ 15 W and working range of it is between 10V and 36V. Activation of the amplifier is provided by a voltage supply of 15.5V given

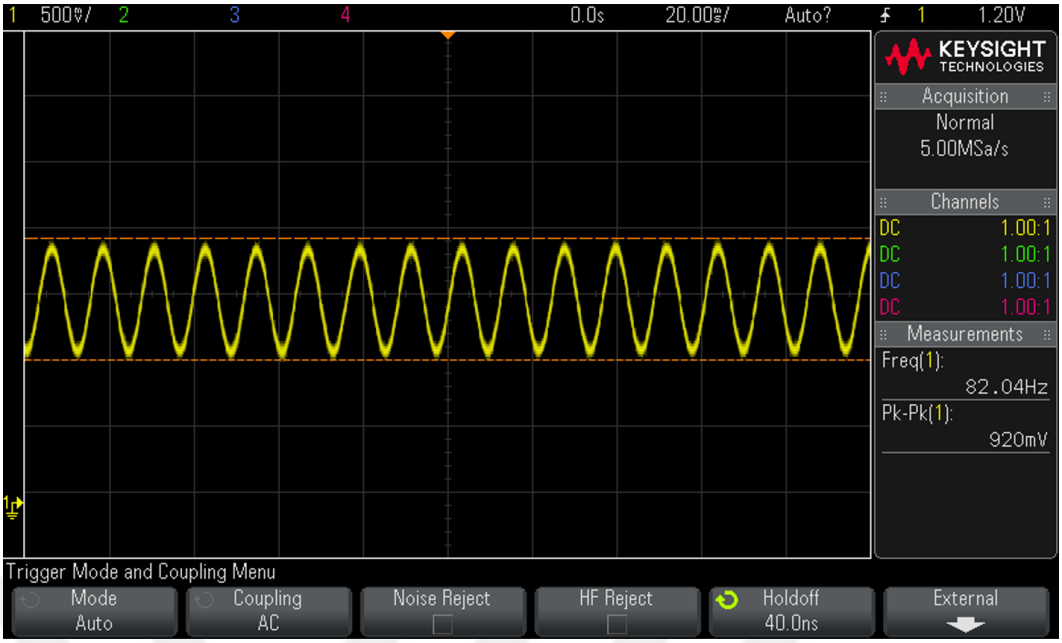

Figure 5.1: Sinusoidal driving output signal in order to drive planar electrocoil that is embedded on microscanner is generated by microcontroller. Signal frequency is 82 Hz and its V_{pp} is 920mV.

from the DC power supply. When the current amplifier (TDA8932) is integrated into the system, it provides current to the planar electrocoil continuously. The voltage and current supplied from current amplifier to the planar electrocoil is 7.1V and 0.067A respectively. This current makes it possible to create an actuation on the microscanner so that one-axis scanning can be performed. Therefore, laser beam is hit the to the polyimide-based microscanner under the maximum magnetic field for a certain period of time. As a consequence of this, the maximum scan angle on the projected surface is achieved for the slow-scan axis having a certain frequency in the system.

The polyimide microscanner enters the resonance state under the influence of the magnetic field applied to the inner frame by the planar electrocoil. In the case of resonance, torsion occurs in the flexures of the scanner, and a significant resistance change (ΔR) occurs as a result of torsion in graphite layers that were previously coated at the point of maximum stress in the flexures of the scanner. The resistance change is transmitted to the read-out circuit through the conductive pads on the scanner. As shown in Figure 5.2, voltage divider that is the most common read-out system work

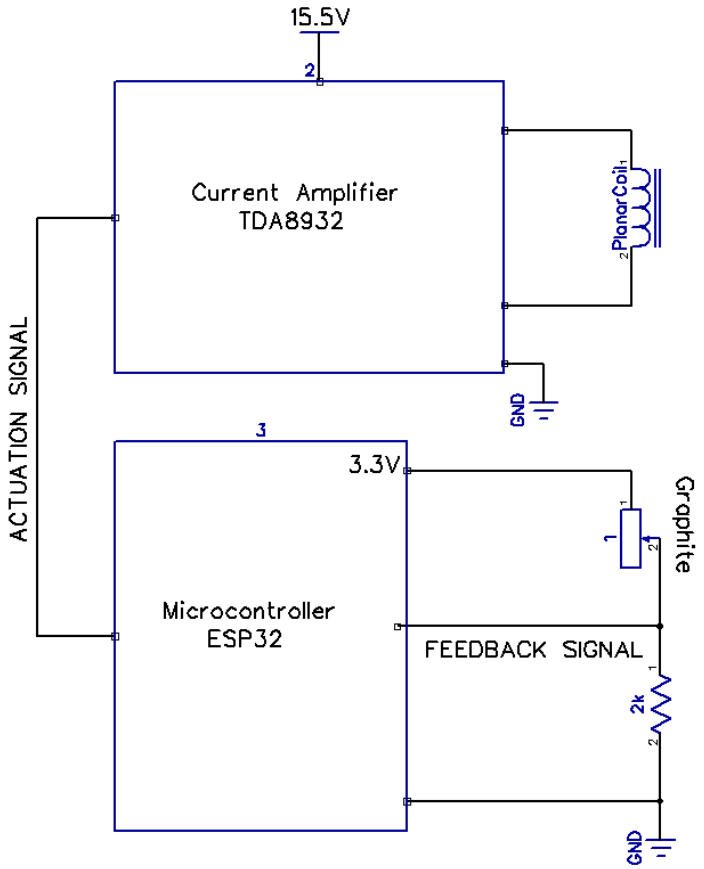

Figure 5.2: The circuit schematic of the embedded system that consists of a Current amplifier (TDA8932), a microcontroller (ESP32) to provide digital signal generation so that slow-scanning is able to be executed, an electrocoil embedded in microscanner to generate magnetic field for actuation, and a subsequent graphite layer for the piezoresistive feedback.

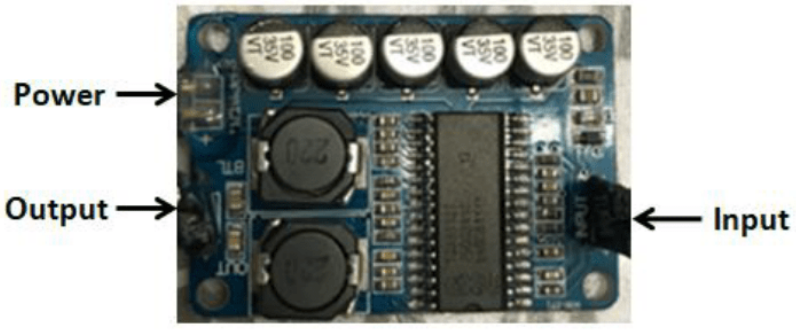

Figure 5.3: View of the current amplifier (TDA 8932).

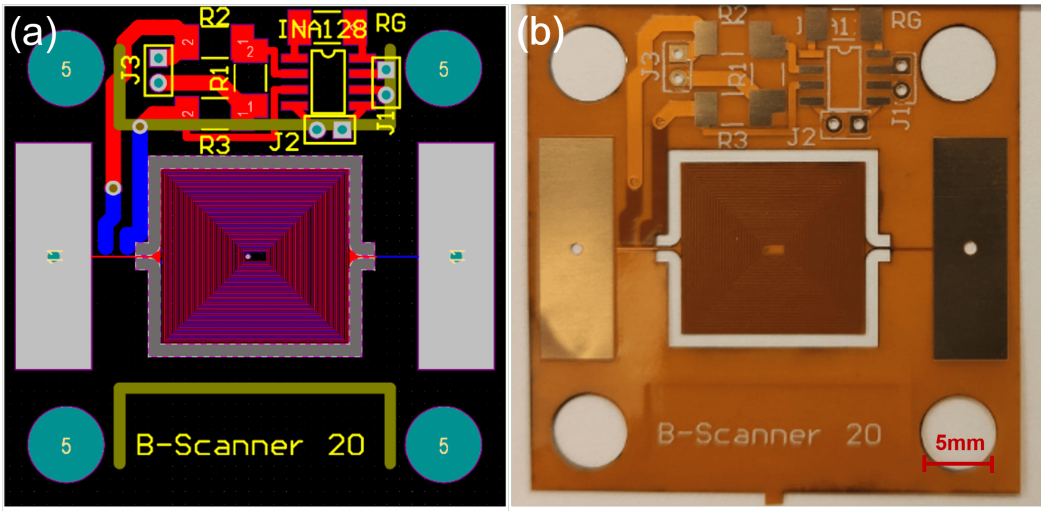

Figure 5.4: (a) top view of pcb schematic of the proposed polyimide-based micro scanner, (b) top view of the printed circuit board (PCB) for the proposed polyimide-based micro scanner. An implemented PCB has dimensions of 40 mm × 40 mm.

on the balance principle is opted as a read-out circuitry. In the circuit indicated, R_{PR}, which tends to vary under the applied mechanical stress is a changeable resistance value and represents the piezoresistive graphite on the flexures of the microscanner. The resistance denoted by R describes the fixed resistance value determined so that the system can start in equilibrium, based on the resistance value of the graphite. R_{PR} is connected between 3.3V pin and the GPIO5 pin of the microcontroller and R is connected between the R_{PR} to ground. In addittion to this, a 10nF ceramic capacitor is placed in parallel with the resistor 2 kΩ. The resistance change of the graphite and signal values can be seen on micro-controller serial plotter.

The proposed polyimide-based microscanner is printed as a flexible printed circuit board as shown in Figures 5.4a and 5.4b. Designs can be made in length and width dimensions of 40 mm × 40 mm, respectively. With the conductive pads on both sides of the device, the necessary current is given to the system to create magnetization. In order to get results on the graphite coated with the flexure, the conductive pad on the relevant side is used in two separate parts and the two parts are used for the ground of the current supplied to the system and the ground of the piezoresistive graphite, respectively.

6. EXPERIMENTS

This chapter elaborates on the experimental works of the fabricated polyimide-based microscanner. Section 6.1 shows the characterization of the microscanner system. Section 6.2 presents experimental results of total optical scan angle (TOSA), spring softening effect, and the piezoresistive feedback system output with various test results.

6.1. Characterization

In following step, the proposed polyimide-based microscanner system is characterized along with laser doppler vibrometer (LDV) and its electronic read-out system.

The system diagram of the characterization test setup is indicated in Figure 6.1. The characterization test setup shown in Figure 6.2 is established over the Thorlabs®optical table to calibrate to the designed and implemented system by means of monitoring its behaviour. The calibration test setup is composed of (1) a 3D stage and a cage plate (Thorlabs®CP02/M-SM1) used to immobilize the scanner structure, (2) Laser Doppler Vibrometer (Polytec®CLV-2534) to transfer displacement information of the vibrating mciroscanner as a form of sinusoidal wave, (3) an oscilloscope (Keysight®InfiniiVision DSOX3054A) to collect the waveform data and shows the peak-to-peak voltage value (V_{pp}), (4) a function generator (Keysight®3321A) to provide the frequency that actuates the microscanner, (5)a versatile multimeter (Agilent®34450A) to view the current flowing through the microscanner.

The characterization setup is installed with its components to monitor the behaviour of the designed and implemented system is shown in Figure 6.2. The polyimide-based microscanner is immobilized first by a cage plate from the outer frame of scanner and then to the optical table by a holder, to eliminate any external movement that could impede the frequency response while in vibration. The Laser-Doppler Vibrometer (LDV) is an instrument that is used to sense the vibration measurements on a

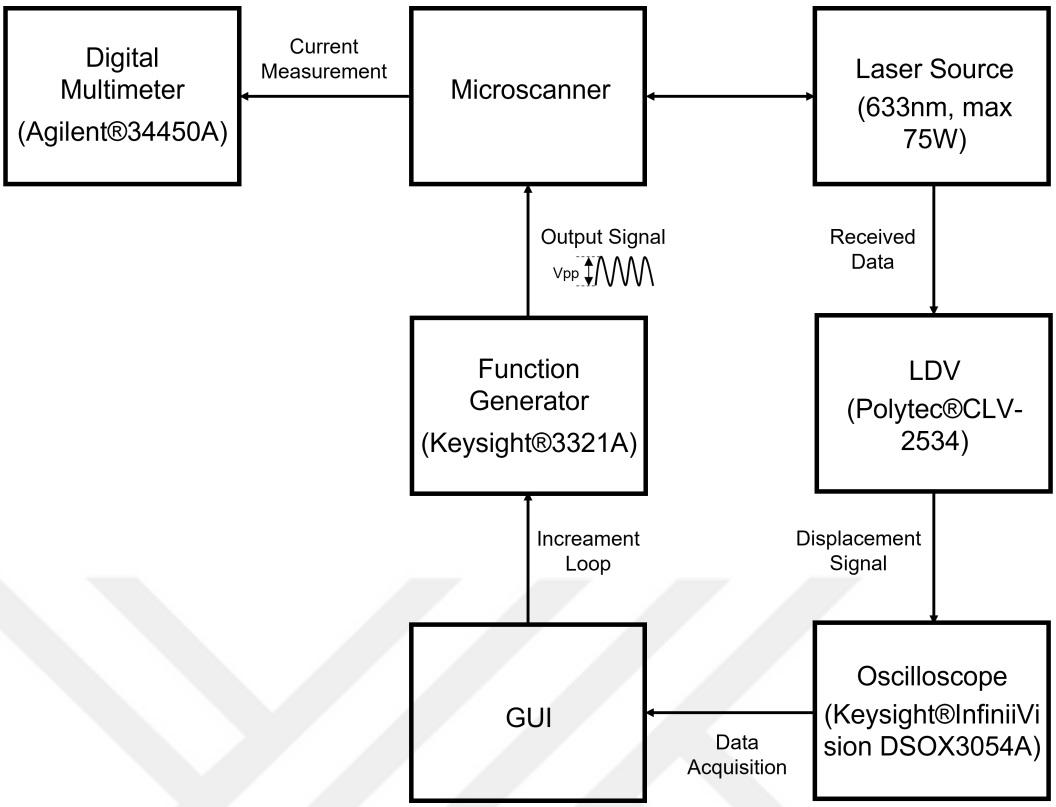

Figure 6.1: The system diagram of the automatized LDV characterization test setup.

reflective object in terms of micrometer. It transfers the displacement information caused by vibration as a form of sinusoidal wave to the oscilloscope in the resolution of 1 volts per 10 nanometers up to 1 volts per 100 centimeters. Subsequently, oscilloscope reads the waveform and displays the peap-to-peak voltage value (V_{pp}). The vibration of the microscanner is provided with the function generator and it send a gradually increasing frequency to the microscanner. With the gradually increasing frequency signal, microscanner starts to actuate and then the resonant frequency of the microscanner is detected. Simultaneously, an increment in V_{pp} value is observed on the oscilloscope. Finally, data which is obtained from experiment process is collected by means of Graphical User Interface (GUI) MATLAB.

The frequency responses of the polyimide-based scanner are plotted below in Figure 6.3, 6.4, and 6.5, respectively. In these characterization tests, LDV laser is reflected over the microscanner in various footprints. The behaviour of the implemented microscanner under the circumstance of right-middle laser reflecting is plotted in Figure

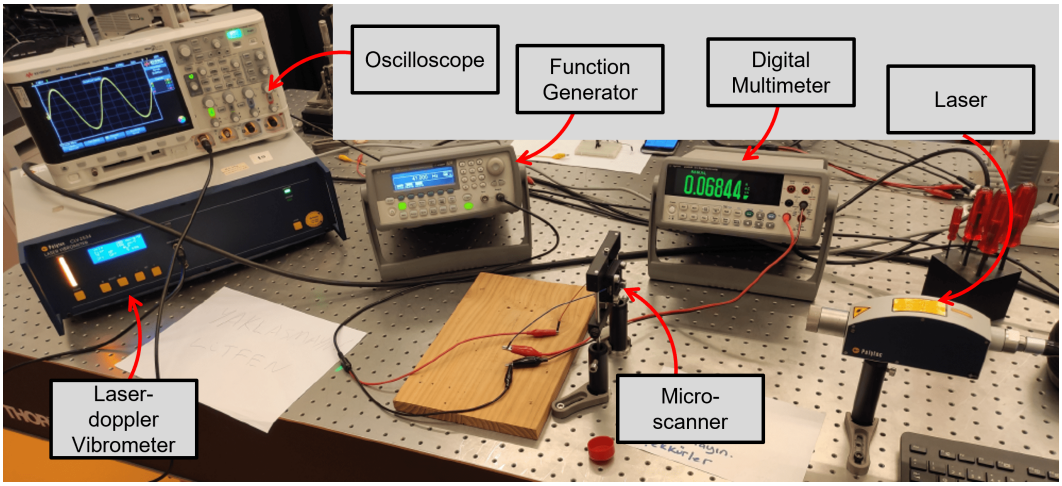

Figure 6.2: View of the LDV characterization test setup to monitor resonant frequency of the proposed microscanner structure in different modes.

6.3. In the experiment, the applied frequency increases from 40 Hz to 1500 Hz with a 5 Hz step size. According to the experiment, when measuring from a point close to the flexures of the scanner with the help of LDV indicated in Figure 6.2, resonance frequency values of the proposed microscanner in different modes where the torsion of the flexures has a prominent effect on the scanner as shown in Figure 3.4 are monitored. As highlighted in Figure 6.3, the acquired resonance frequency values are 60 Hz, 285 Hz, 685 Hz, 1290 Hz, and 1460 Hz, respectively. In the 50-70 Hz range, the scanner reaches its maximum scanning aperture.

In Figure 6.4, the polyimide-based microscanner is observed under the circumstance of middle laser reflecting. The experiment was carried out by performing the frequency value from 40 Hz to 1500 Hz with a step size of 0.1 Hz. Within the scope of this experiment, measurement is made from the middle point on the A-A' axis, which is the slow scanning axis of the scanner, via LDV. As a result of the measurements made, the frequency value at which the microscanner resonates is observed as 285 Hz. Comparing the simulation result that is shown in Figure 3.4 and the characterization result in Figure 6.4, the error percentage between the results obtained for mode (B) is below 15%. It's safe to say that this error is largely due to the slightly varying size of the scanner dimensions, as the laser cutting process is not very precise.

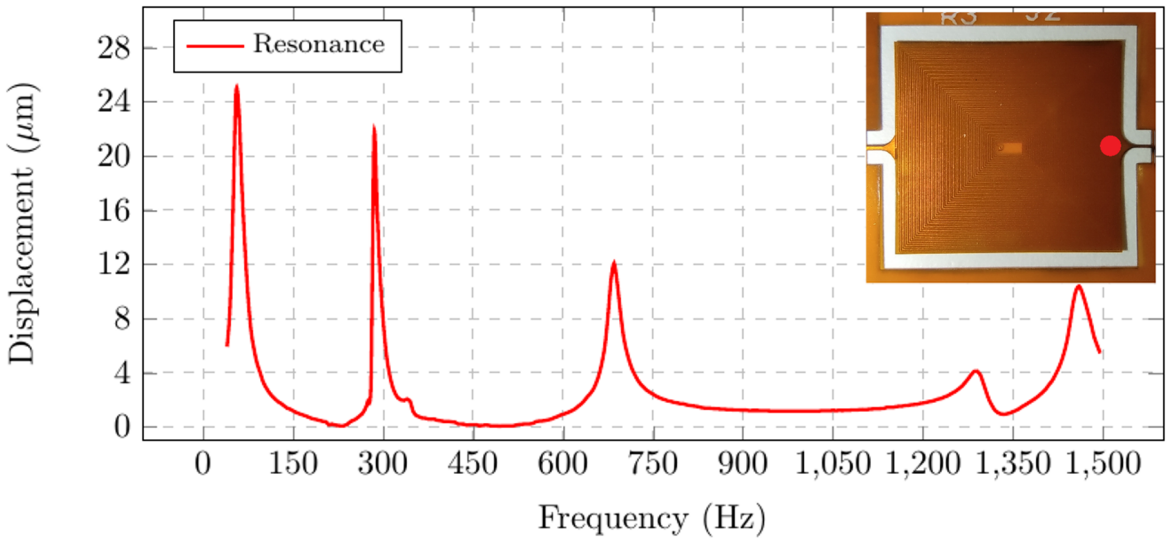

Figure 6.3: A characterization graph of the polyimide-based microscanner shows the saturation behaviours of the proposed scanner in different modes by plotting the incremental frequency versus the displacement.

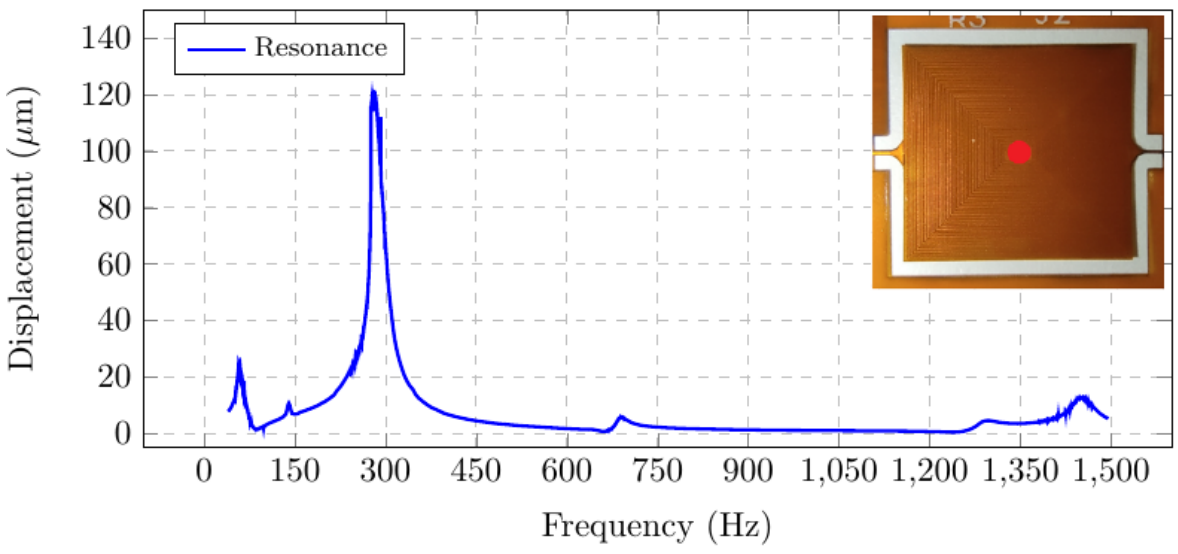

Figure 6.4: A characterization graph of the polyimide-based microscanner shows the saturation behaviour of the proposed scanner in mode (B) by plotting the incremental frequency versus the displacement.

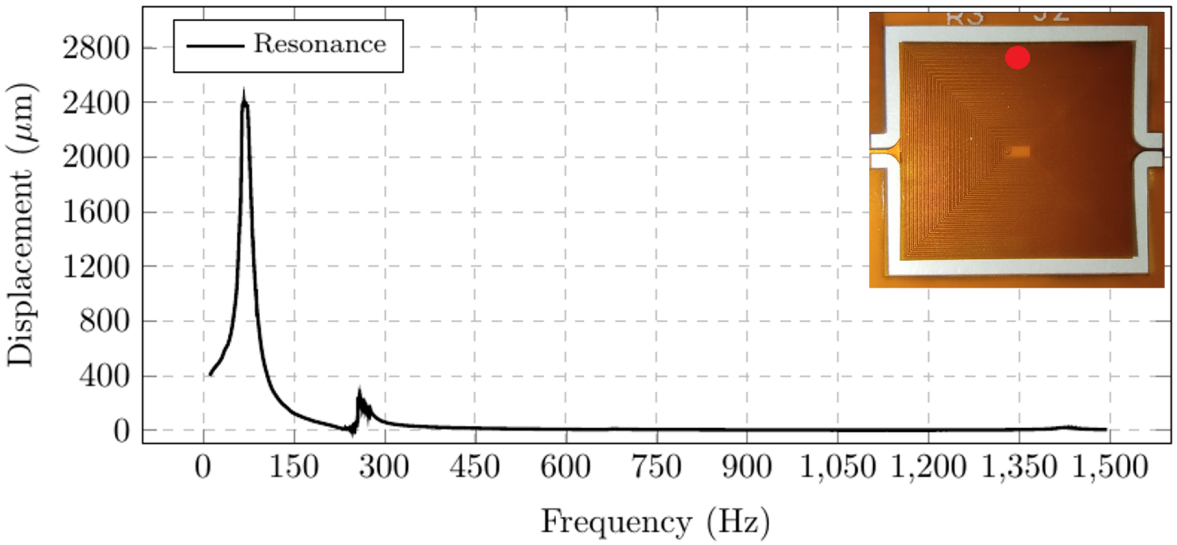

Figure 6.5: A characterization graph of the polyimide-based microscanner shows the saturation behaviour of the proposed scanner in mode (A) by plotting the incremental frequency versus the displacement.

Finally, the calibration test indicated in Figure 6.5 is carried out for the motion mode that resonates at the lowest slow-scan frequency value desired to be determined within the scope of this study. As indicated at the top right of the plot, the experiment is performed by holding the scanner constant along the slow scanning axis A-A' and measuring the point where the amount of torsional displacement is highest. The operating range frequency value of the experiment is between 40 Hz and 1500 Hz with a step size of 0.1 Hz. As a result of the obtained characterization test result, the peak point with the highest displacement of the scanner is determined as 68 Hz. Comparing the simulation results shown in Figure 3.4 with this experiment, the error percentage between the results obtained for mode (A) is below 20%. The reasons for this error are able to be stated as follows: the change in the dimensions of the scanner due to laser cutting, and the inability to correspond to the exact edge of the scanner due to the fact that the point focus of the laser source is not very sensitive.

According to these experimental results, our proposed scanner structure is calibrated with LDV as an optical process related to the amount of displacement versus frequency change. Thus, the information at which frequency the scanner resonates, and hence saturate, is obtained.

6.2. Test Results

In the following step, the proposed polyimide-based microscanner having a piezoresistive feedback system is tested along with its electronic read-out circuit as shown in Figure 6.6. The experimental test setup is established over the Thorlabs®optical table and it is used to test piezoresistive graphite feedback of the proposed polyimide-based microscanner, and real-time feedback circuit assembly that can be used for closed-loop scanning systems. It harbors eight components. These are (1) a polyimide-based microscanner structure whose top surfaces of its flexures are coated with thin-film piezoresistive layers, and anchored with a 3D stage and a cage plate (Thorlabs®CP02/M-SM1), (2) a feedback circuitry composed of a conventional voltage divider to detect changes in resistance due to stress caused by flexure buckling on the piezoresistive graphite layers, (3) a generic ESP32 micro-controller (ESP32-WROOM-32) generating a signal to drive the microscanner, (4) a current amplifier (TDA9832) to drive the planar electrocoil, (5) 5 mW laser-source (RYS1230) with 650nm wavelength along with its custom-made switching circuitry, (6) a power supply (Keysight®E3620A) to drive the current amplifier, (7) a neodymium magnet to increase the magnetic field onto the scanner, and finally a PC to monitor and process these data is installed.

The setup is installed with its components to monitor the behaviour of the scanner system is shown in Figure 6.6 in terms of piezoresistive feedback. The polyimide-based microscanner having a piezoresistive feedback is fixed between the cage plate to avoid external vibrational movements that may affect the frequency response during the actuation. Within the experiment, the digital signal generated from the microcontroller is connected directly from the digital to analog (DAC) output to the input of the current amplifier. Amplifier is worked with 15.5V and 0.45A. The output of the amplifier is connected to the microscanner to amplify the output current of the ESP32 to operate the electrocoil on the scanner. After the electrocoil is activated, a neodymium magnet is placed under the scanner to increase the magnetic field that enables the scanner, whose flexures are coated with graphite layer. As a result, the scanner undergoes a torsional motion which increases the stress level in its flexures and creates a certain

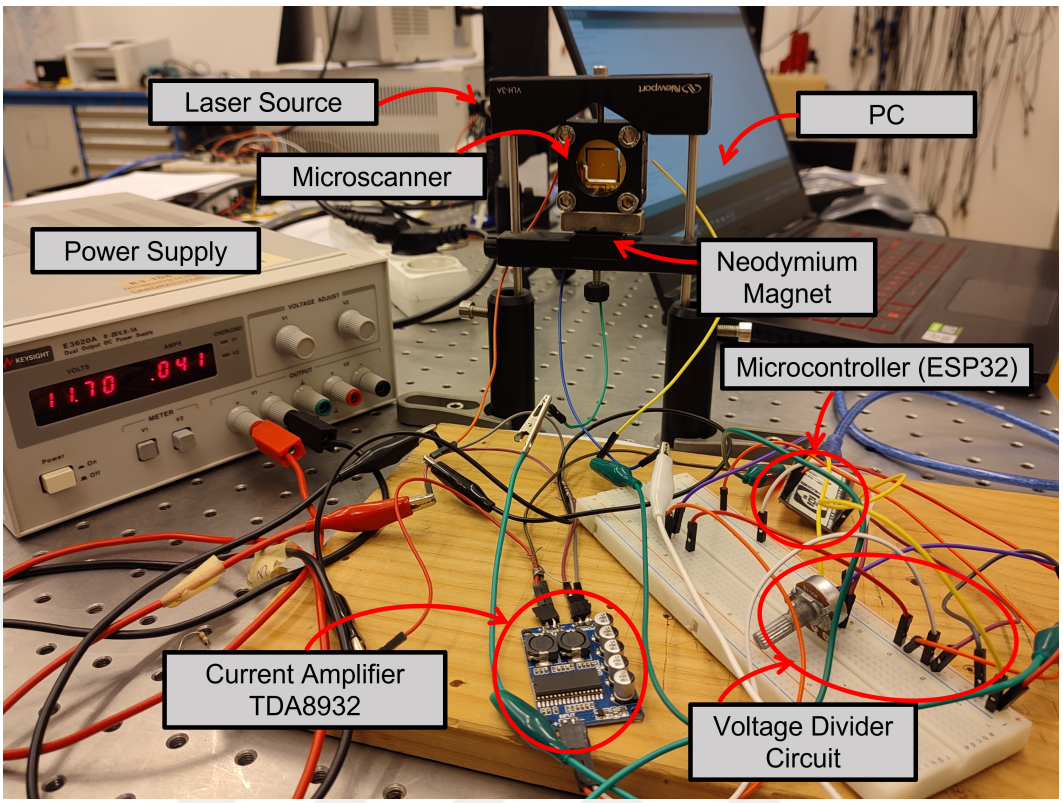

Figure 6.6: View of the experimental test setup used to monitor the TOSA and create a closed-loop by providing a feedback to the frequency response obtained through graphite.

planar scanning angle shown inside in Figure 6.8.

It has been explained in the previous sections that the stress level occurring in the flexures of the polyimide-based microscanner increases proportionally to the magnitude of the torsional motion and TOSA illustrated in Figure 6.7, and hence to the amount of deflection caused by the slow scanning made by the polyimide-based structure. Thus, the resistance changes occurring in the graphite coated over the flexures with high torsion are monitored as voltage change ratio data via a read-out circuit. For this purpose, it is aimed to determine the normalized voltage change ($\Delta V/V$) value corresponding to the frequency response and saturation point of the microscanner. In addition to this, it is desired to ensure that the scanner always remains at the saturation point with piezoresistive feedback.

Total optical scan angle can be calculated by the Equation 6.1, where A is length

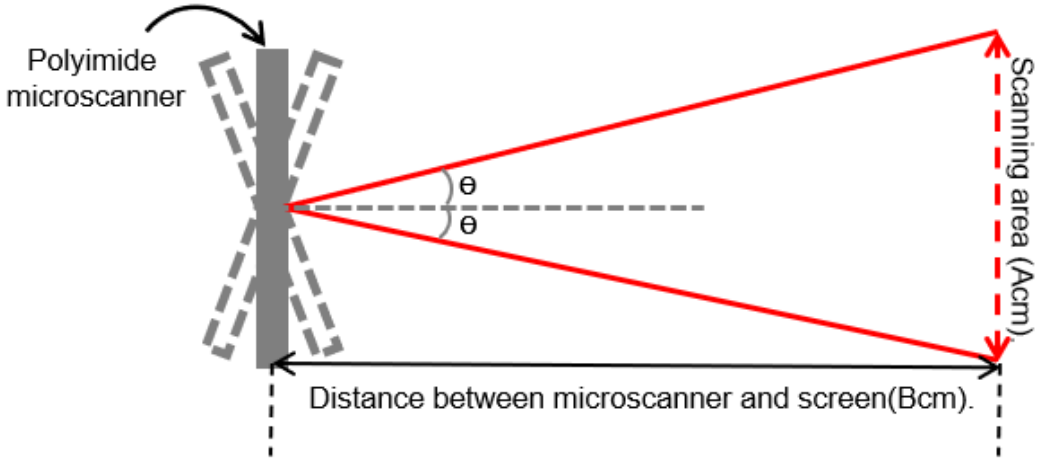

Figure 6.7: Illustration of the scanner emphasizing the scanner movement, angle θ, scanning area, and distance between microscanner and screen.

of the scanning area, θ is angle, and B is the distance between scanner and scanned are. In Figure 6.7, length of the scanned area is related to width and scan angle. The subsequent experiment gives the values of the TOSA value, where the amount of given frequency is gradually increased and correspondingly changing. The given frequency is increased from 40 Hz to 100 Hz with a step size of approximately 1 Hz. The changes in the TOSA values of the proposed microscanner structure versus given frequency are plotted in Figure 6.8. According to the experimental result shown in Figure 6.8, TOSA is determined as 73.59° at the resonance frequency of 82 Hz.

$$TOSA = 2\theta, \theta = arctan((A/2)/B) \tag{6.1}$$

The resonance frequency of the microscanner varies depending on fabrication errors, mechanical fatigue, temperature, and pressure factors. Since the scanner is constantly loaded with current, the temperature effect from the specified parameters plays an important role. Analyzes performed on MEMS instruments help accurately predict nonlinear states in the instrument, such as spring softening and hardening

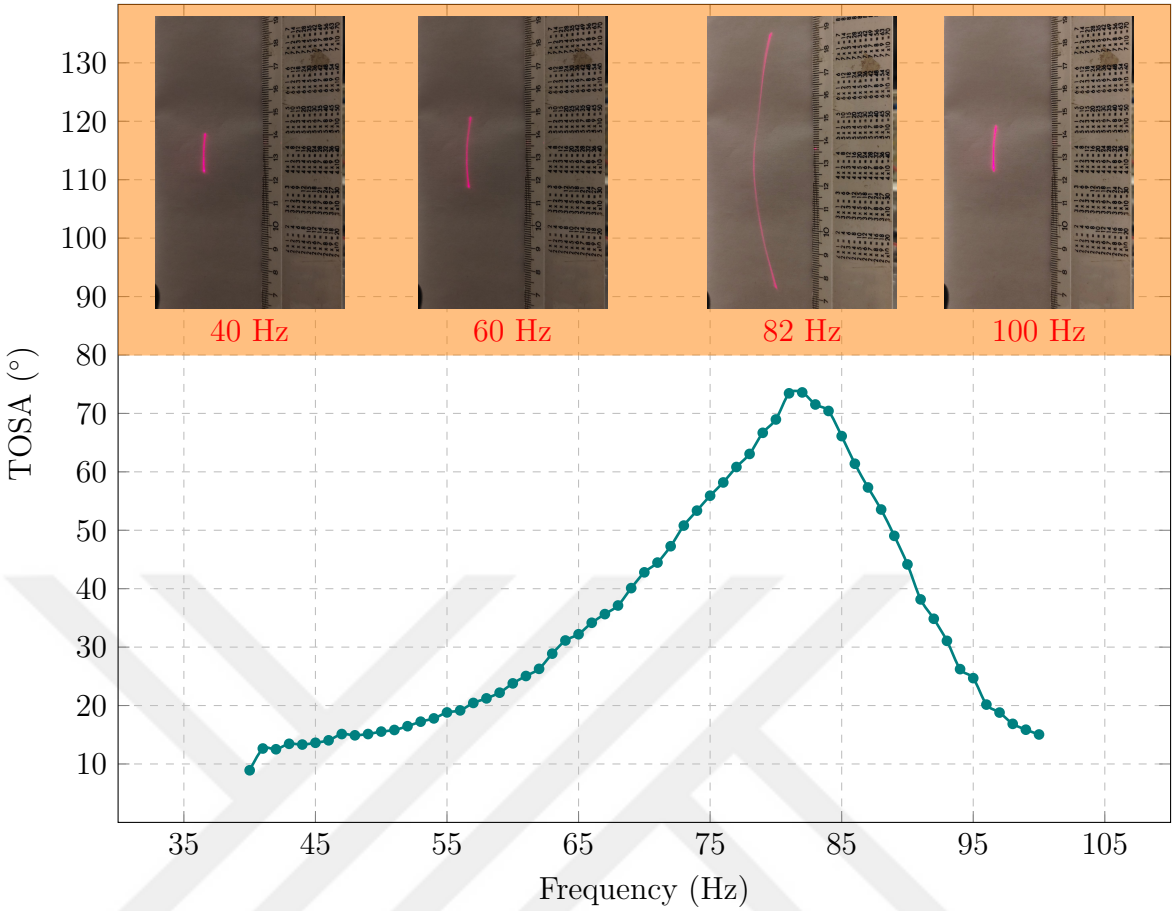

Figure 6.8: A graph of the total optical scanning angle (TOSA) of the microscanner during operation, along with scanned angle images taken at different frequency values in it, shows the behavior of changes in scan angle as a function of frequency change.

effect [90]. The spring softening effect is a reduction in the effective spring constant. This effect produces a reduction in the resonant frequency [91]. Spring hardening is the opposite of this effect: there is an increase in the effective spring constant. On the other hand, usually one of the two effects dominates. Applying voltage to the planar electrocoil embedded into the polyimide scanner to generate electromagnetic motion reduces the resonance frequency due to the spring softening property of the material.

An experiment was carried out to determine the softening effect and its the root mean squared error (RMSE) with an LDV measurement. The related experiment gives the values of the saturation points and the displacement amount, where the amount of supplied power is gradually increased and correspondingly changing. The supplied

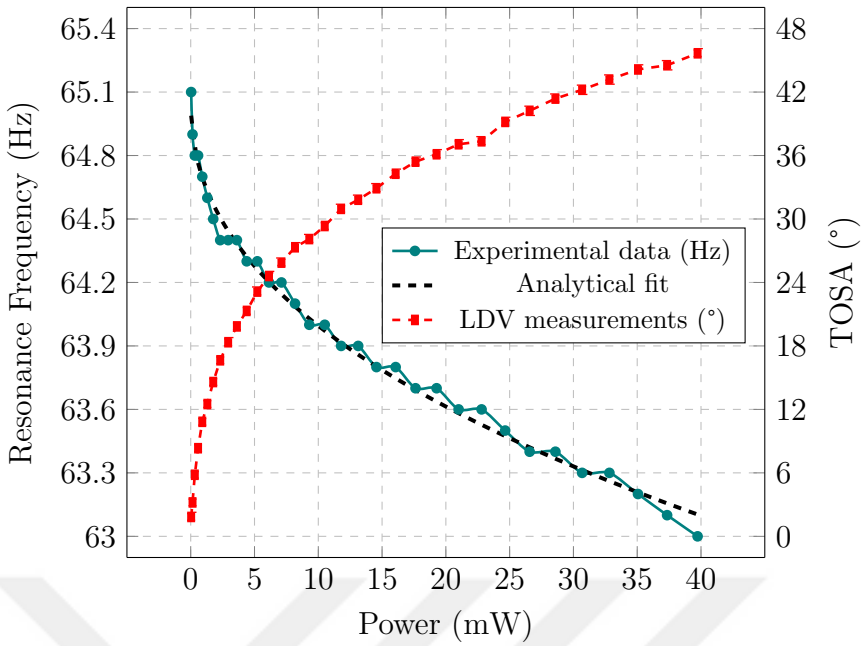

Figure 6.9: A graph of the softening effect of the microscanner while getting actuated shows the behavior of the proposed scanner structure in terms of temperature by plotting the changes in the resonance frequency value and TOSA value versus the supplied power. The dashed line in this part represents the analytical fitted equation of $y = -0.3984x^{0.435} + 65.08$ with an R-squared value of 0.9928, and RMSE value of 0.04939.

power is changed from 0 mW to 40 mW with a step size of approximately 1.5 mW. The changes in the resonance frequency and TOSA values of the proposed microscanner structure versus supplied power are plotted in Figure 6.9. The change in resonance frequency is reported decrease exponentially from 65.1 Hz to 63.0 Hz. However, it is reported that the TOSA value increased inversely from 1.83° to 45.66°. In the same Figure, the black and dashed line denotes the curve fitting starting between 65.1 and 63.0 Hz. The range behaviour of this scanner is able to be modelled with $y = -0.3984x^{0.435} + 65.08$ with an R-squared value of 0.9928, and RMSE value of 0.04939.

According to this experimental result, it is seen that the amount of displacement on the microscanner increases as the current to the planar electrocoil increases, whereas it reaches the high displacement amount at a lower frequency. This phenomenon can be

explained as a decrease in the spring constant as well as softening effect of the spring.

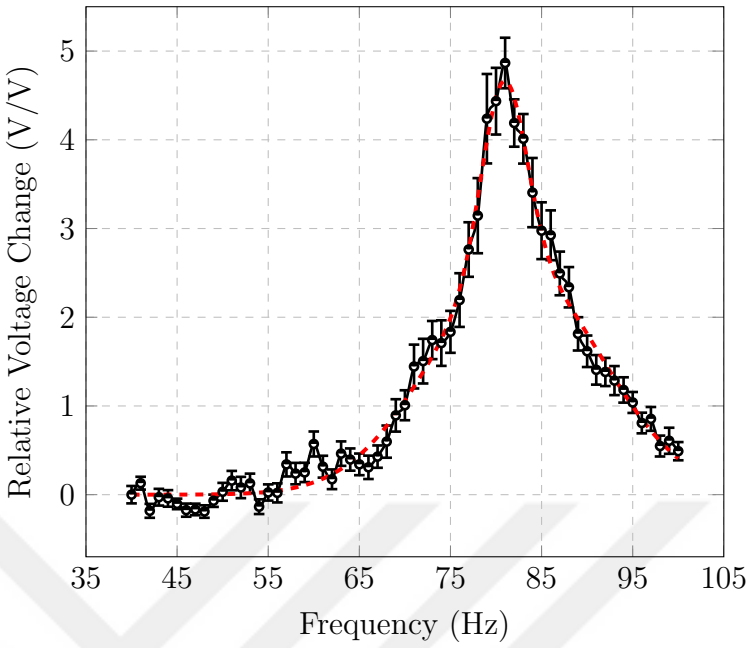

Figure 6.10: The behavior of polyimide-based microscanner coated with graphite layer. The dashed line in this part represents the analytical fitted equation of $y = 2.126e^{(-((x-80.88)/3.42)^2)} + 2.567e^{(-((x-82.29)/13.06)^2)}$ with an R-squared value of 0.9866, and RMSE value of 0.1632.

The subsequent experiment was performed by gradually increasing the frequency within the detected resonance frequency range of the scanner characterization tests to determine whether the microscanner could perform piezoresistive feedback with precision and to determine the root mean square error (RMSE). The related experiment gives the behavior of the normalized voltage change that occurs in the graphite layer coated on the flexures of the microscanner, in which the amount of frequency given to the system gradually increases. In this way, the maximum displacement information of the scanner, which develops depending on the frequency, and the saturation point information from there are obtained. The frequency given to the system is increased from 40 Hz to 100 Hz with a step size of 1 Hz. The changes in the normalized voltage ΔV/V of the graphite layer versus given frequency are plotted in Figure 6.10. The maximum normalized voltage change in graphite occurs in the 81 Hz frequency and is reported as 4.866 V/V. Therewithal, the optical scanning angle (TOSA) is calculated as 73.59°. The average error margins for the proposed scanner is measured as 0.173

V/V. As emphasized in the Figure 6.10, the red and dashed line expresses the analytical fitting as Gaussian function starting from 40 Hz, rising to 81 Hz, and descending back to 100 Hz. Also, its average sensitivity is defined as 5.835 (mV/°) from the 40 Hz initial position to the saturation point of 81 Hz and 3.0 (mV/°) from the peak to 100 Hz. The behaviour is can be modelled with $y = 2.126e^{(-((x-80.88)/3.42)^2)} + 2.567e^{(-((x-82.29)/13.06)^2)}$ with an R-squared value of 0.9866, and RMSE value of 0.1632.

As a result of this experiment, it can be read that the polyimide-based microscanner is in resonance with the feedback from the graphite at the highest point of the scanning range. The point at which the scan angle is highest corresponds to the highest peak value in the graph. When FEM analyzes and experimental results were compared, it is seen that consistent results were obtained. Thus, a real-time feedback system is obtained.

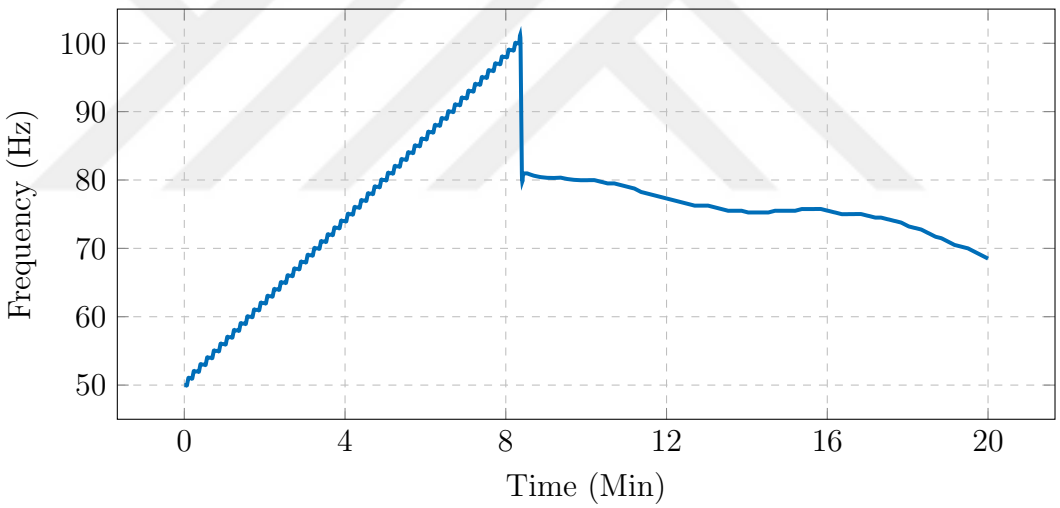

Figure 6.11: The auto-tuned behavior of polyimide-based microscanner coated with graphite layer.

In order to make an auto-tuned system, C code was developed. The code and the experimental results are shown in Appendix C and Figure 6.11, respectively. Initially, the actuation signal is given to the scanner from 50 Hz to 100 Hz with a step size of 1 Hz. The maximum amplitude value is obtained by capturing and comparing each frequency value with piezoresistive feedback signals obtained. The maximum amplitude value indicates the frequency value at which the microscanner is in resonance and is

given to the microscanner. As a result, the microscanner starts to operate at maximum scanning aperture. However, over a certain period of time, the scanner heats up and then a shift in the resonant frequency of the scanner occurs due to the spring softening effect. In order to detect the shifted frequency and to maintain the maximum scanning aperture and hence resonant mode of the scanner continuously, the system has been auto-tuned by means of a code developed as mentioned above. In the developed system, while the resonant frequency value is given to the system, the resonant frequency value is increased by 2 Hz and decreased by 2 Hz in the background. Thus, the current feedback signal is compared with the signals obtained from the previous and subsequent frequency values, and if a higher feedback signal is obtained as a result of this, the current frequency value at which the maximum amplitude value is obtained is given to the system. According to the results of the experiment shown in Figure 6.11, the resonance frequency was determined as 81 Hz in the first step, and it was observed that the resonance frequency decreased to 78 Hz after the scanner had been operated for 15 minutes.

7. DISCUSSION

In this study, a low-cost, and having a low-energy consumption microscanner is designed and implemented to ensure the compact system that has piezoresistive feedback, and the robustness against to the plastic deformation under the torsional movements. In this regard, polyimide was chosen as the main substrate material and it was reported that the polyimide-based scanner structure is sensitive, low-cost and durable enough to be used in feedback systems due to the flexibility of the material, its ability to reach high apertures, and its ability to be easily magnetized at low frequencies.

As described in the sections above, in this study, a polyimide-based scanner structure with an embedded planar electrocoil, and its flexure coated with graphite for piezoresistive feedback is proposed as a new method.In this way, the resonance frequency is precisely determined by the piezoresistive feedback provided by graphite with a low error.

In this study, using this proposed feedback methodology, a sufficiently sensitive structure was developed compared to the FR4-based scanner [55] and the stainless steel scanner [53]. By using a flexible, low-cost substrate material in the proposed polyimide-based microscanner structure, lower energy consumption and lower resonance frequency, higher TOSA and sensitivity are achieved compared to other studies. A brief comparison between this thesis and the studies reported in [55], and [53] is given in Table 7.1.

Considering the above-mentioned factors, some innovations and improvements can be made on the system. These can be listed as follows: (1) the reading circuit of the system can be placed on the scanner structure, making it a monolithic system, (2) a more sensitive reading circuit can be designed, (3) the system can be made automatic adjustment, (4) a light-sensing system can be integrated for bioscanning.

Table 7.1: Comparison of specifications of our proposed polyimide-based microscanner regarding its structural and geometric, actuation and feedback type, driving device, and obtained results, to the other works.

Specifications	**This work**	**Reference [55]**	**Reference [53]**
Substrate Material	Polyimide (150 μm thick)	FR4 (500 μm thick)	Stainless Steel
Array Size (L × w × t) (mm)	15 × 14 × 0.15	12 × 2 × 0.5	22.6 × 22.6 × -
Inner Mirror Geometry	Rectangular	Square	Circular
Scanning Dimension	one-dimensional (1D)	one-dimensional (1D)	two-dimensional (2D)
Actuation Type	Electromagnetic (1D)	Electromagnetic (1D)	Electromagnetic (2D)
Electrocoil Type	Integrated Planar Electrocoil	Integrated Planar Electrocoil	External Coil
Feedback Type	Piezoresistive Feedback	Angle Sensor	Position Sensitive Device
Electrocoil Driving Device	Microcontroller (ESP32)	Function Generator	Function Generator
Driving Power (mW)	475.7	-	200
Driving Voltage (mV)	7100	420	-
Resonance Frequency	81 Hz	361.8 Hz	112 Hz
TOSA	73.59°	22.4°	20.6°
Sensitivity	5.835 mV/°	40.70281 mV/°	-
BoM	4.2$	-	-

8. CONCLUSION

In this thesis, a polyimide-based microscanner system was designed, implemented, and characterized. For closed-loop systems, a piezoresistive feedback mechanism is created using implemented scanner structure. Furthermore, the system is auto-tuned to maintain the resonant mode. The main susbtrate material of the proposed 15 mm $\times$ 14 mm scanner is a 150μm thick polyimide and the sensing material is graphite (Bare Conductive®Electric Paint). A thin-film piezoresistive graphite paste is coated to the point where the scanner structure flexures were most stressed in order to more precisely detect the saturation frequency. In addition, the scanner can generate more scanning angles and torsional motions by effective displacement thanks to the proposed polyimide-based structure, which is constructed in the narrowest and most durable manner within the scanner's design constraints. This further increases the sensitivity of the system. The proposed microscanner structure is actuated with an embedded electrocoil that is triggered by an external magnet. Experiments shows that the microscanner has a TOSA of 73.59° in the slow-scan direction, with the optical scanning angle of the Polyimide-based scanner at approximately 82 Hz, as tabulated in Table 7.1. Also, the saturation point frequency from real-time piezoresistive feedback is about 81 Hz. The average error rate result is 0.173 V/V. At the same time, its average sensitivity is defined as 5.835 (mV/°) from the 40 Hz initial position to the 81 Hz saturation point and 3.0 (mV/°) from the peak to 100 Hz.

Each part of the system is controlled simultaneously using an ESP32 microcontroller. In conclusion, the results show that the proposed system can work well in a closed-loop system. As a feature of future studies, the sensor is produced for use in distinguishing an biologic structure.

REFERENCES

1. Mishra, M. K., V. Dubey, P. Mishra and I. Khan, "MEMS technology: A review", *J. Eng. Res. Rep*, Vol. 4, No. 1, pp. 1–24, 2019.

2. Hwang, K., Y.-H. Seo and K.-H. Jeong, "Microscanners for optical endomicroscopic applications", *Micro and Nano Systems Letters*, Vol. 5, No. 1, pp. 1–11, 2017.

3. Li, H., Z. Qiu, X. Duan, K. R. Oldham, K. Kurabayashi and T. D. Wang, "2D resonant microscanner for dual axes confocal fluorescence endomicroscope", *2014 IEEE 27th International Conference on Micro Electro Mechanical Systems (MEMS)*, pp. 805–808, IEEE, 2014.

4. Yan, J., S. Luanava and V. Casasanta, "Magnetic actuation for MEMS scanners for retinal scanning displays", *MOEMS Display and Imaging Systems*, Vol. 4985, pp. 115–120, SPIE, 2003.

5. Schwarz, F., F. Senger, J. Albers, P. Malaurie, C. Janicke, L. Pohl, F. Heinrich, D. Kaden, H.-J. Quenzer, F. Lofink *et al.*, "Resonant 1D MEMS mirror with a total optical scan angle of 180° for automotive LiDAR", *MOEMS and Miniaturized Systems XIX*, Vol. 11293, pp. 46–62, SPIE, 2020.

6. Ye, L., G. Zhang and Z. You, "Large-aperture kHz operating frequency Ti-alloy based optical micro scanning mirror for LiDAR application", *Micromachines*, Vol. 8, No. 4, p. 120, 2017.

7. Li, H., X. Duan, Z. Qiu, Q. Zhou, K. Kurabayashi, K. R. Oldham and T. D. Wang, "Integrated monolithic 3D MEMS scanner for switchable real time vertical/horizontal cross-sectional imaging", *Optics express*, Vol. 24, No. 3, pp. 2145–2155, 2016.

8. Schenk, H., M. Wagner, J. Grahmann and A. Merten, "Advances in MOEMS

technologies for high quality imaging systems", *Optical Microlithography XXXI*, Vol. 10587, p. 1058703, SPIE, 2018.

9. Frigerio, P., R. Tarsi, L. Molinari, G. Maiocchi, A. Barbieri and G. Langfelder, "A novel closed-loop architecture for accurate micromirror trajectory control in linear scanning MEMS-based projectors", *MOEMS and Miniaturized Systems XX*, Vol. 11697, pp. 23–32, SPIE, 2021.

10. Wakunami, K., P.-Y. Hsieh, R. Oi, T. Senoh, H. Sasaki, Y. Ichihashi, M. Okui, Y.-P. Huang and K. Yamamoto, "Projection-type see-through holographic three-dimensional display", *Nature communications*, Vol. 7, No. 1, pp. 1–7, 2016.

11. Hollemann, G., B. Braun, P. Heist, J. Symanowski, U. Krause, J. Kraenert and C. Deter, "High-power laser projection displays", *Projection Displays VII*, Vol. 4294, pp. 36–46, SPIE, 2001.

12. Lin, H.-C. and Y.-H. Lin, "An electrically tunable focusing pico-projector adopting a liquid crystal lens", *Japanese journal of applied physics*, Vol. 49, No. 10R, p. 102502, 2010.

13. Sandner, T., C. Baulig, T. Grasshoff, M. Wildenhain, M. Schwarzenberg, H.-G. Dahlmann and S. Schwarzer, "Hybrid assembled micro scanner array with large aperture and their system integration for a 3D ToF laser camera", *MOEMS and Miniaturized Systems XIV*, Vol. 9375, p. 937505, SPIE, 2015.

14. Sandner, T., T. Grasshoff, M. Schwarzenberg and H. Schenk, "Quasi-static microscanner with linearized scanning for an adaptive 3D-laser camera", *2013 International Conference on Optical MEMS and Nanophotonics (OMN)*, pp. 103–104, IEEE, 2013.

15. Van Kessel, P. F., L. J. Hornbeck, R. E. Meier and M. R. Douglass, "A MEMS-based projection display", *Proceedings of the IEEE*, Vol. 86, No. 8, pp. 1687–1704, 1998.

16. Perreault, J. A., T. G. Bifano, B. M. Levine and M. N. Horenstein, "Adaptive optic correction using micro-electro-mechanical deformable mirrors", *Optical Engineering*, Vol. 41, No. 3, pp. 561–566, 2002.

17. Chen, R., H. Nguyen and M. Wu, "A high-speed low-voltage stress-induced micromachined 2 x 2 optical switch", *IEEE Photonics Technology Letters*, Vol. 11, No. 11, pp. 1396–1398, 1999.

18. Ataman, Ç. and H. Urey, "Compact Fourier transform spectrometers using FR4 platform", *Sensors and Actuators A: Physical*, Vol. 151, No. 1, pp. 9–16, 2009.

19. Ferhanoglu, O., H. R. Seren, S. Lüttjohann and H. Urey, "Lamellar grating optimization for miniaturized fourier transform spectrometers", *Optics express*, Vol. 17, No. 23, pp. 21289–21301, 2009.

20. Kumar, K., K. Hoshino and X. Zhang, "Handheld subcellular-resolution single-fiber confocal microscope using high-reflectivity two-axis vertical combdrive silicon microscanner", *Biomedical microdevices*, Vol. 10, No. 5, pp. 653–660, 2008.

21. Hofmann, U., S. Muehlmann, M. Witt, K. Doerschel, R. Schuetz and B. Wagner, "Electrostatically driven micromirrors for a miniaturized confocal laser scanning microscope", *Miniaturized Systems with Micro-Optics and MEMS*, Vol. 3878, pp. 29–38, SPIE, 1999.

22. Von Reischach, F., S. Karpischek, F. Michahelles and R. Adelmann, "Evaluation of 1D barcode scanning on mobile phones", *2010 Internet of Things (IOT)*, pp. 1–5, IEEE, 2010.

23. Goda, K., K. K. Tsia and B. Jalali, "Amplified dispersive Fourier-transform imaging for ultrafast displacement sensing and barcode reading", *Applied Physics Letters*, Vol. 93, No. 13, p. 131109, 2008.

24. Duma, V.-F., "Laser scanners with oscillatory elements: Design and optimization

of 1D and 2D scanning functions", *Applied Mathematical Modelling*, Vol. 67, pp. 456–476, 2019.

25. Pohl, L., F. Schwarz, P. Blicharski, C. Janicke, O. Petrak, T. von Wantoch and U. Hofmann, "Wide angle LiDAR demonstrator based on a resonantly operated 1D MEMS mirror capable of scanning 180", *MOEMS and Miniaturized Systems XX*, Vol. 11697, pp. 89–105, SPIE, 2021.

26. Schenk, H., P. Duerr, D. Kunze, H. K. Lakner and H. Kueck, "Design and modeling of large deflection micromechanical 1D and 2D scanning mirrors", *MOEMS and Miniaturized Systems*, Vol. 4178, pp. 116–125, SPIE, 2000.

27. Druml, N., I. Maksymova, T. Thurner, D. van Lierop, M. Hennecke and A. Foroutan, "1D MEMS micro-scanning LiDAR", *Conference on Sensor Device Technologies and Applications (SENSORDEVICES)*, Vol. 9, 2018.

28. Armstrong, E. and R. Richmond, "The application of inverse filters to 3D microscanning of LADAR imagery", *2006 IEEE Aerospace Conference*, pp. 6–pp, IEEE, 2006.

29. Myaing, M. T., D. J. MacDonald and X. Li, "Fiber-optic scanning two-photon fluorescence endoscope", *Optics letters*, Vol. 31, No. 8, pp. 1076–1078, 2006.

30. Csencsics, E. and G. Schitter, "System design and control of a resonant fast steering mirror for lissajous-based scanning", *IEEE/ASME Transactions on Mechatronics*, Vol. 22, No. 5, pp. 1963–1972, 2017.

31. Seo, Y.-H., K. Hwang, H. Kim and K.-H. Jeong, "Scanning MEMS mirror for high definition and high frame rate Lissajous patterns", *Micromachines*, Vol. 10, No. 1, p. 67, 2019.

32. Urey, H., D. W. Wine and T. D. Osborn, "Optical performance requirements for MEMS-scanner-based microdisplays", *MOEMS and Miniaturized Systems*, Vol.

4178, pp. 176–185, SPIE, 2000.

33. Teo, Y. R., Y. Yong and A. J. Fleming, "A comparison of scanning methods and the vertical control implications for scanning probe microscopy", *Asian Journal of control*, Vol. 20, No. 4, pp. 1352–1366, 2018.

34. Atabak, R., H. M. Sedighi, A. Reza and E. Mirshekari, "Instability analysis of bi-axial micro-scanner under electromagnetic actuation including small scale and damping effects", *Microsystem Technologies*, Vol. 26, No. 8, pp. 2615–2638, 2020.

35. Yalcinkaya, A. D., H. Urey, D. Brown, T. Montague and R. Sprague, "Two-axis electromagnetic microscanner for high resolution displays", *Journal of Microelectromechanical Systems*, Vol. 15, No. 4, pp. 786–794, 2006.

36. Cho, A. R., A. Han, S. Ju, H. Jeong, J.-H. Park, I. Kim, J.-U. Bu and C.-H. Ji, "Electromagnetic biaxial microscanner with mechanical amplification at resonance", *Optics express*, Vol. 23, No. 13, pp. 16792–16802, 2015.

37. Urey, H., S. Holmstrom and A. D. Yalcinkaya, "Electromagnetically actuated FR4 scanners", *IEEE Photonics Technology Letters*, Vol. 20, No. 1, pp. 30–32, 2007.

38. Ji, C.-H., M. Choi, S.-C. Kim, K.-C. Song, J.-U. Bu and H.-J. Nam, "Electromagnetic two-dimensional scanner using radial magnetic field", *Journal of microelectromechanical systems*, Vol. 16, No. 4, pp. 989–996, 2007.

39. Schroth, A., C. Lee, S. Matsumoto, M. Tanaka and R. Maeda, "Application of sol-gel deposited thin PZT film for actuation of 1D and 2D scanners", *Proceedings MEMS 98. IEEE. Eleventh Annual International Workshop on Micro Electro Mechanical Systems. An Investigation of Micro Structures, Sensors, Actuators, Machines and Systems (Cat. No. 98CH36176*, pp. 402–407, IEEE, 1998.

40. Cheng, H.-C., S.-C. Liu, C.-C. Hsu, H.-Y. Lin, F. Shih, M. Wu, K.-C. Liang, M.-F. Lai and W. Fang, "On the design of piezoelectric MEMS scanning mirror for

large reflection area and wide scan angle", *Sensors and Actuators A: Physical*, p. 114010, 2022.

41. Rombach, S., M. Marx, S. Gu-Stoppel and Y. Manoli, "Low power and highly precise closed-loop driving circuits for piezoelectric micromirrors with embedded capacitive position sensors", *MOEMS and Miniaturized Systems XV*, Vol. 9760, pp. 140–150, SPIE, 2016.

42. Matsushita, S., I. Kanno, R. Yokokawa and H. Kotera, "Metal-based piezoelectric MEMS scanner mirrors composed of PZT thin films on titanium substrates", *2011 16th International Solid-State Sensors, Actuators and Microsystems Conference*, pp. 574–577, IEEE, 2011.

43. Tanguy, Q. A., S. Bargiel, H. Xie, N. Passilly, M. Barthès, O. Gaiffe, J. Rutkowski, P. Lutz and C. Gorecki, "Design and fabrication of a 2-axis electrothermal mems micro-scanner for optical coherence tomography", *Micromachines*, Vol. 8, No. 5, p. 146, 2017.

44. Struk, P., S. Bargiel, Q. Tanguy, F. G. Ramirez, N. Passilly, P. Lutz, O. Gaiffe, H. Xie and C. Gorecki, "Swept-source optical coherence tomography microsystem with an integrated Mirau interferometer and electrothermal micro-scanner", *Optics Letters*, Vol. 43, No. 19, pp. 4847–4850, 2018.

45. Li, L., R. Bauer, G. Brown and D. Uttamchandani, "A symmetric hybrid MEMS scanner with electrothermal and electrostatic actuators", *16th International Conference on Optical MEMS and Nanophotonics*, pp. 163–164, IEEE, 2011.

46. Schenk, H., H. Conrad, M. Gaudet, S. Uhlig, B. Kaiser, S. Langa, M. Stolz and K. Schimmanz, "A novel electrostatic micro-actuator class and its application potential for optical mems", *2016 International Conference on Optical MEMS and Nanophotonics (OMN)*, pp. 1–2, IEEE, 2016.

47. Chen, Y., H. Li, Z. Qiu, T. D. Wang and K. R. Oldham, "Improved extended

Kalman filter estimation using threshold signal detection with an MEMS electrostatic microscanner", *IEEE Transactions on Industrial Electronics*, Vol. 67, No. 2, pp. 1328–1336, 2019.

48. Ishikawa, N., K. Ikeda and R. Sawada, "Temperature dependence of the scanning performance of an electrostatic microscanner", *Journal of Micromechanics and Microengineering*, Vol. 26, No. 3, p. 035002, 2016.

49. Isikman, S. O. and H. Urey, "Dynamic modeling of soft magnetic film actuated scanners", *IEEE transactions on magnetics*, Vol. 45, No. 7, pp. 2912–2919, 2009.

50. Holmström, S. T., U. Baran and H. Urey, "MEMS laser scanners: a review", *Journal of Microelectromechanical Systems*, Vol. 23, No. 2, pp. 259–275, 2014.

51. Pal, P. and K. Sato, *Silicon wet bulk micromachining for MEMS*, Jenny Stanford Publishing, 2017.

52. Kim, S., C. Lee, J. Y. Kim, G. Lim, J. Kim and C. Kim, "A 2-axis Polydimethylsiloxane (PDMS) based electromagnetic MEMS scanning mirror for optical coherence tomography", *Advanced Biomedical and Clinical Diagnostic and Surgical Guidance Systems XIV*, Vol. 9698, pp. 100–105, SPIE, 2016.

53. Wang, Y., Y. D. Gokdel, N. Triesault, L. Wang, Y.-Y. Huang and X. Zhang, "Magnetic-actuated stainless steel scanner for two-photon hyperspectral fluorescence microscope", *Journal of Microelectromechanical Systems*, Vol. 23, No. 5, pp. 1208–1218, 2014.

54. Oyman, H., M. Icel, B. Efe, Y. Gokdel, O. Ferhanoglu and A. Yalcinkaya, "A laser-machined stainless-steel micro-scanner for confocal microscopy", *Multidisciplinary Digital Publishing Institute Proceedings*, Vol. 1, No. 4, p. 564, 2017.

55. Lei, H., Q. Wen, F. Yu, Y. Zhou and Z. Wen, "FR4-based electromagnetic scanning micromirror integrated with angle sensor", *Micromachines*, Vol. 9, No. 5, p. 214,

2018.

56. Isikman, S. O., R. B. Sprague and H. Urey, "FR4 laser scanner with dynamic focus", *IEEE Photonics Technology Letters*, Vol. 21, No. 4, pp. 233–235, 2008.

57. Periyasamy, K. G., H. Zuo and S. He, "Flexible printed circuit board magnetic micromirror for laser marking/engraving", *Journal of Micromechanics and Microengineering*, Vol. 29, No. 8, p. 085001, 2019.

58. Schroedter, R., K. Janschek and T. Sandner, "Jerk and current limited flatness-based open loop control of foveation scanning electrostatic micromirrors", *IFAC Proceedings Volumes*, Vol. 47, No. 3, pp. 2685–2690, 2014.

59. Frigerio, P., M. Gianollo, G. Pezzi, L. Molinari, A. Barbieri, M. Zamprogno, R. Carminati, N. Boni and G. Langfelder, "Mitigating Hysteresis Effects in Open-Loop-Driven PZT MEMS Micromirrors with Piezoresistive Sensing", *2021 21st International Conference on Solid-State Sensors, Actuators and Microsystems (Transducers)*, pp. 1100–1103, IEEE, 2021.

60. Schroedter, R., T. Sandner, K. Janschek, M. Roth and C. Hruschka, "Real-time closed-loop control for micro mirrors with quasistatic comb drives", *MOEMS and Miniaturized Systems XV*, Vol. 9760, pp. 28–40, SPIE, 2016.

61. Pannu, S., C. Chang, R. Muller and A. Pisano, "Closed-loop feedback-control system for improved tracking in magnetically actuated micromirrors", *2000 IEEE/LEOS International Conference on Optical MEMS (Cat. No. 00EX399)*, pp. 107–108, IEEE, 2000.

62. Schroedter, R., M. Schwarzenberg, A. Dreyhaupt, R. Barth, T. Sandner and K. Janschek, "Microcontroller based closed-loop control of a 2D quasi-static/resonant microscanner with on-chip piezo-resistive sensor feedback", *MOEMS and Miniaturized Systems XVI*, Vol. 10116, pp. 22–32, SPIE, 2017.

63. Lin, H., T.-W. Lin, A. C.-L. Hung and M. S.-C. Lu, "A bi-axial capacitive scanning mirror with closed-loop control", *2018 IEEE Micro Electro Mechanical Systems (MEMS)*, pp. 567–570, IEEE, 2018.

64. Ghazinouri, B., S. He and T. S. Tai, "A position sensing method for 2D scanning mirrors", *Journal of Micromechanics and Microengineering*, Vol. 32, No. 4, p. 045007, 2022.

65. Cagdaser, B., A. Jog, M. Last, B. S. Leibowitz, L. Zhou, E. Shelton, K. S. Pister and B. E. Boser, "Capacitive sense feedback control for MEMS beam steering mirrors", *Proc. of Solid-State Sensor, Actuator and Microsystems Workshop, Hilton Head Island, South Carolina, USA, June*, pp. 6–10, 2004.

66. Grahmann, J., H. Conrad, T. Sandner, T. Klose and H. Schenk, "Integrated position sensing for 2D microscanning mirrors using the SOI device layer as the piezoresistive mechanical-elastic transformer", *MOEMS and Miniaturized Systems VIII*, Vol. 7208, pp. 61–70, SPIE, 2009.

67. Wen, Q., H. Lei, F. Yu, D. Li, Y. She, J. Huang, L. Huang and Z. Wen, "Investigation of electromagnetic angle sensor integrated in FR4-based scanning micromirror", *Applied Sciences*, Vol. 8, No. 12, p. 2412, 2018.

68. Zhou, Y., Q. Wen, Z. Wen, J. Huang and F. Chang, "An electromagnetic scanning mirror integrated with blazed grating and angle sensor for a near infrared micro spectrometer", *Journal of Micromechanics and Microengineering*, Vol. 27, No. 12, p. 125009, 2017.

69. Tortschanoff, A., M. Baumgart, A. Frank, M. Wildenhain, T. Sandner, H. Schenk and A. Kenda, "Optical position feedback for electrostatically driven MOEMS scanners", *MOEMS and Miniaturized Systems XI*, Vol. 8252, pp. 216–223, SPIE, 2012.

70. Baumgart, M., M. Lenzhofer, M. Kremer and A. Tortschanoff, "Integrated pack-

aging of 2D MOEMS mirrors with optical position feedback", *MOEMS and Miniaturized Systems XIV*, Vol. 9375, pp. 176–182, SPIE, 2015.

71. Lani, S., D. Bayat and M. Despont, "2D MEMS scanner integrating a position feedback", *MATEC Web of Conferences*, Vol. 32, p. 01001, EDP Sciences, 2015.

72. Ozturk, A., H. I. Ocakli, N. Ozber, H. Urey, I. H. Kavakli and B. E. Alaca, "A magnetically actuated resonant mass sensor with integrated optical readout", *IEEE Photonics Technology Letters*, Vol. 20, No. 23, pp. 1905–1907, 2008.

73. Duan, C., W. Wang, X. Zhang, L. Zhou, A. Pozzi and H. Xie, "A self-aligned 45°-tilted two-axis scanning micromirror for side-view imaging", *Journal of Microelectromechanical Systems*, Vol. 25, No. 4, pp. 799–811, 2016.

74. Wang, D., C. Watkins, S. Koppal and H. Xie, "A silicon optical bench with vertically-oriented micromirrors for active beam steering", *Sensors and Actuators A: Physical*, Vol. 298, p. 111586, 2019.

75. Urey, H., "Torsional MEMS scanner design for high-resolution scanning display systems", *Optical Scanning 2002*, Vol. 4773, pp. 27–37, SPIE, 2002.

76. Luo, Y., M. R. Abidian, J.-H. Ahn, D. Akinwande, A. M. Andrews, M. Antonietti, Z. Bao, M. Berggren, C. A. Berkey, C. J. Bettinger *et al.*, "Technology Roadmap for Flexible Sensors", *ACS nano*, 2023.

77. Liu, C., *Foundations of MEMS*, Pearson Education India, 2012.

78. Işikman, S. Ö., *Electromagnetically actuated optical micro-mechatronic systems integrated on PCB*, Master's Thesis, Fen Bilimleri Enstitüsü, 2008.

79. Bayat, D., C. Ataman, B. Guldimann, S. Lani, W. Noell and N. F. de Rooij, "Large electrostatically and electromagnetically actuated mirror system for space applications", *2010 International Conference on Optical MEMS and Nanophotonics*, pp.

193–194, IEEE, 2010.

80. Sasada, I. and Y. Nakashima, "Planar coil system consisting of three coil pairs for producing a uniform magnetic field", *Journal of applied physics*, Vol. 99, No. 8, p. 08D904, 2006.

81. Matsuki, H., N. Fujii, K. Shirakawa, J. Toriu and K. Murakami, "Magnetic-multi-turn planar coil inductor", *IEEE transactions on magnetics*, Vol. 27, No. 6, pp. 5438–5440, 1991.

82. Pacurar, C., V. Topa, A. Racasan and C. Munteanu, "Inductance calculation and layout optimization for planar spiral inductors", *2012 13th International Conference on Optimization of Electrical and Electronic Equipment (OPTIM)*, pp. 225–232, IEEE, 2012.

83. Poliakine, J., Y. Civet and Y. Perriard, "Design and manufacturing of high inductance planar coils for small scale sensing applications", *Procedia Engineering*, Vol. 168, pp. 1127–1130, 2016.

84. Liyuan, Y., L. Shushu, N. Pingjuan, S. Hao, M. Run and C. Zheng, "Novel square spiral Coil for achieving uniform Distribution of magnetic Field", *IOP Conference Series: Earth and Environmental Science*, Vol. 332, p. 042005, IOP Publishing, 2019.

85. Erman, M. F. and V. T. Kilic, "Magnetic Field Calculation of Square Coils Having Rounded Corners", *2019 1st Global Power, Energy and Communication Conference (GPECOM)*, pp. 212–215, IEEE, 2019.

86. Aebischer, H., "Inductance formula for rectangular planar spiral inductors with rectangular conductor cross section", *Advanced Electromagnetics*, Vol. 9, No. 1, pp. 1–18, 2020.

87. Bouanou, T., H. El Fadil, A. Lassioui, O. Assaddiki and S. Njili, "Analysis of coil

parameters and comparison of circular, rectangular, and hexagonal coils used in WPT system for electric vehicle charging", *World Electric Vehicle Journal*, Vol. 12, No. 1, p. 45, 2021.

88. Misakian, M., "Equations for the magnetic field produced by one or more rectangular loops of wire in the same plane", *Journal of research of the National Institute of Standards and Technology*, Vol. 105, No. 4, p. 557, 2000.

89. Kraus, J. D., D. A. Fleisch and S. H. Russ, "Electromagnetics with applications", , 1999.

90. Johnson, S., "Experimental analysis of spring hardening and softening nonlinearities in microelectromechanical oscillators.", .

91. Elshurafa, A. M., K. Khirallah, H. H. Tawfik, A. Emira, A. K. A. Aziz and S. M. Sedky, "Nonlinear dynamics of spring softening and hardening in folded-MEMS comb drive resonators", *Journal of Microelectromechanical Systems*, Vol. 20, No. 4, pp. 943–958, 2011.

APPENDIX A: DATASHEETS

A.1. Bare Conductive®Electric paint

Bare Conductive® Electric Paint®

Technical Data Sheet
English

PRODUCT DESCRIPTION

Electric Paint is a nontoxic, water based, water soluble, electrically conductive paint. It can be used in circuits as a painted resistor element, a capacitive electrode or can function as a conductor in designs that can tolerate high resistivity. It is intended for applications with circuits using low DC voltages at low currents. **Electric Paint** adheres to a wide variety of substrates and can be applied using screen printing equipment. Its major benefits include low cost, solubility in water and good screen life. It is black in colour and can be over-painted with any material compatible with a water-based paint.

ADVANTAGES / PRODUCT BENEFITS

- High sheet resistance
- Nontoxic
- Water-soluble
- Can be used to create capacitive touch and proximity sensors
- Can be used as a potentiometer or resistive circuit element
- Compatible with many standard screen printing processes
- Low cost

TYPICAL PROPERTIES

Colour /	Black
Viscosity /	Highly viscous and shear sensitive (thixotropic)
Density /	1.16 g/ml
Sheet Resistance /	55Ω/sq at 50 micron film thickness
Vehicle /	Water-based
Drying Temperature /	**Electric Paint** should be allowed to dry at room temperature for 5 – 15 minutes. Drying time can be reduced by placing Electric Paint under a warm lamp or other low intensity heat source.

See below summary table of typical properties.

PROCESSING AND HANDLING

Screen Printing Equipment /	Manual
Screen Types /	Polyester, stainless steel (43T – 90T gauge mesh)
Typical Cure Conditions /	Room temperature (24˚C) for 15 minutes
Typical Circuit Line Width /	0.5 – 10mm (43T-mesh stainless steel screen)
Clean-up Solvent /	Warm water and soap
Sheet Resistance /	Approximately 32Ω/sq when using a brush or manual screen printing
Shelf Life /	6 months after opening
Storage /	**Electric Paint** should be stored, tightly sealed in a clean, stable environment at room temperature. Composition should be thoroughly mixed prior to use.

See below graph to predict resistance using manual screen printing.

First Floor, 98 Commercial St
London E1 6LZ, United Kingdom
+44 0 207 650 7977
info@bareconductive.com

A.2. Thorlabs®CP02/M-SM1 Cage Plate

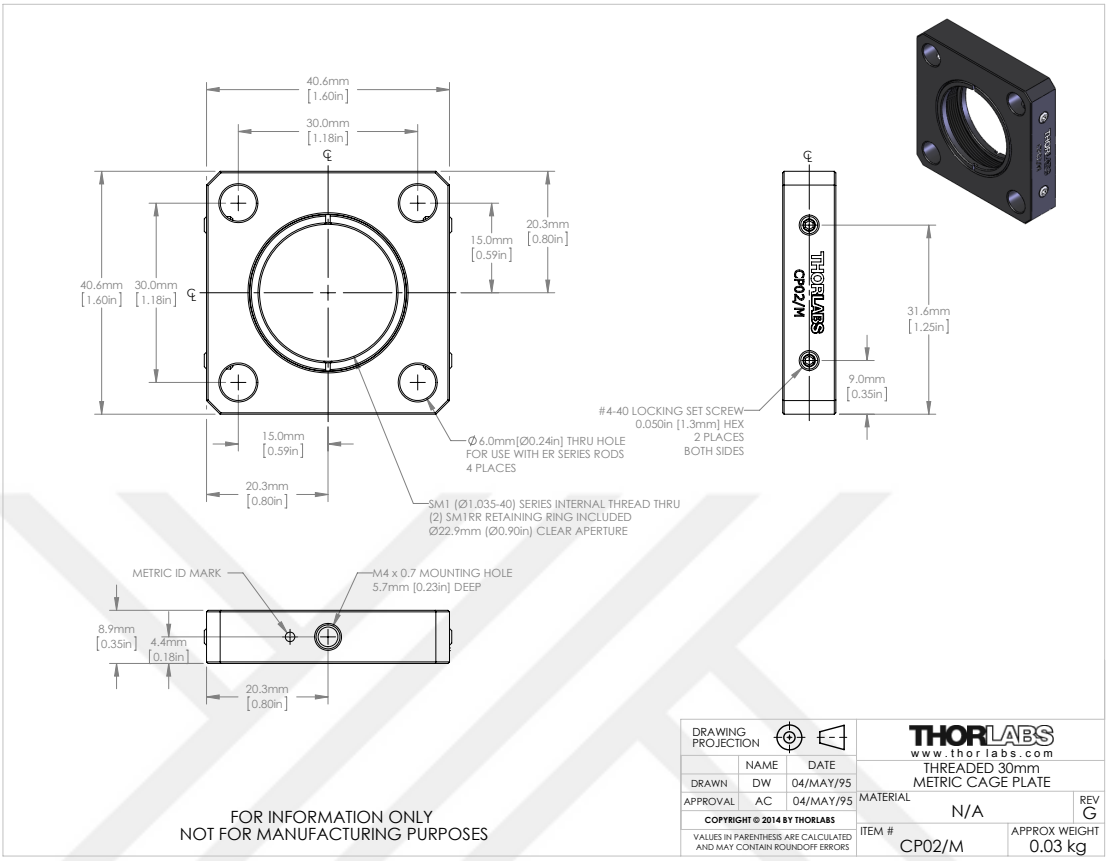

A.3. TDA8932 Class-D Type Power Amplifier

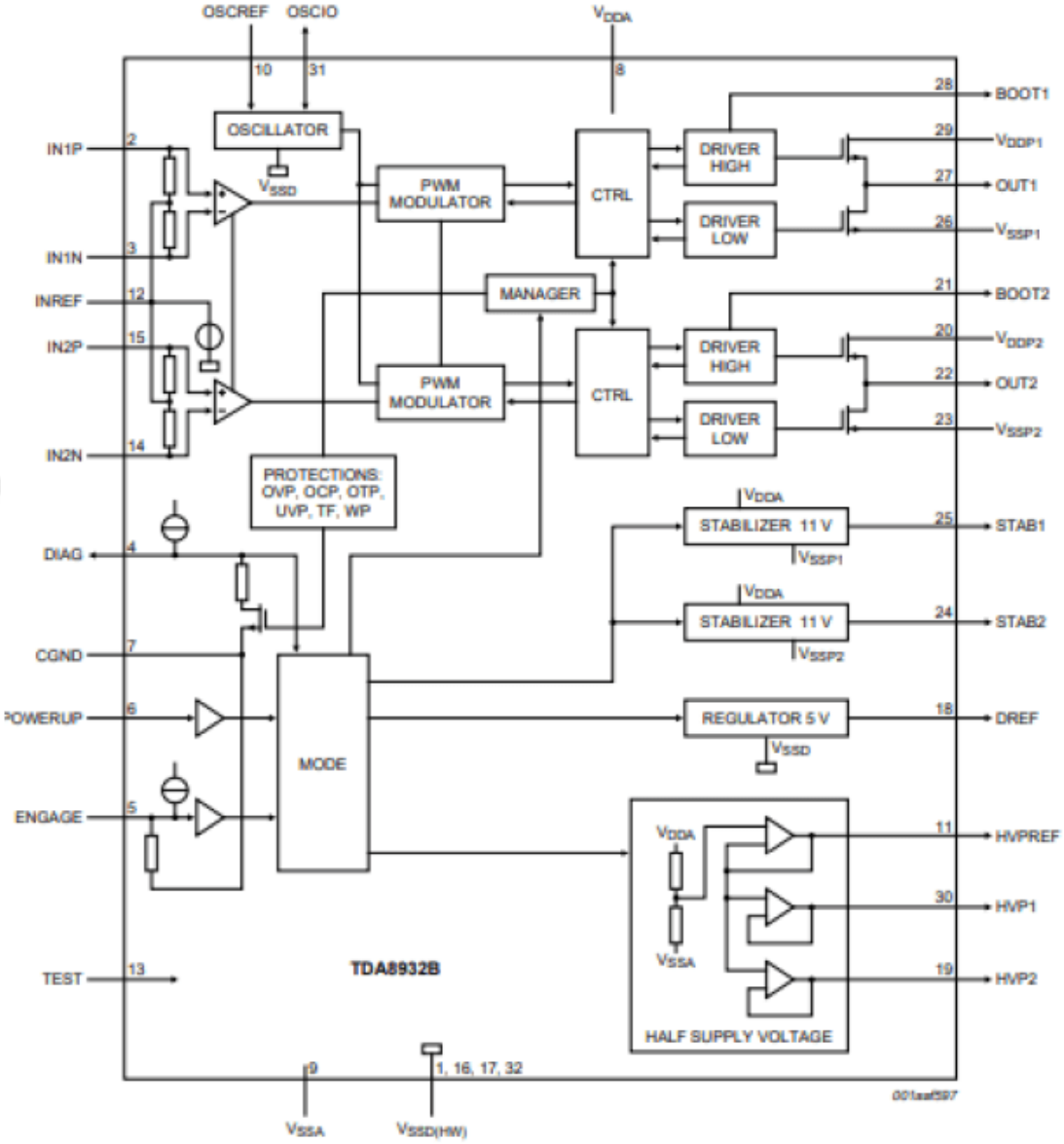

A.4. ESP32 Microcontroller

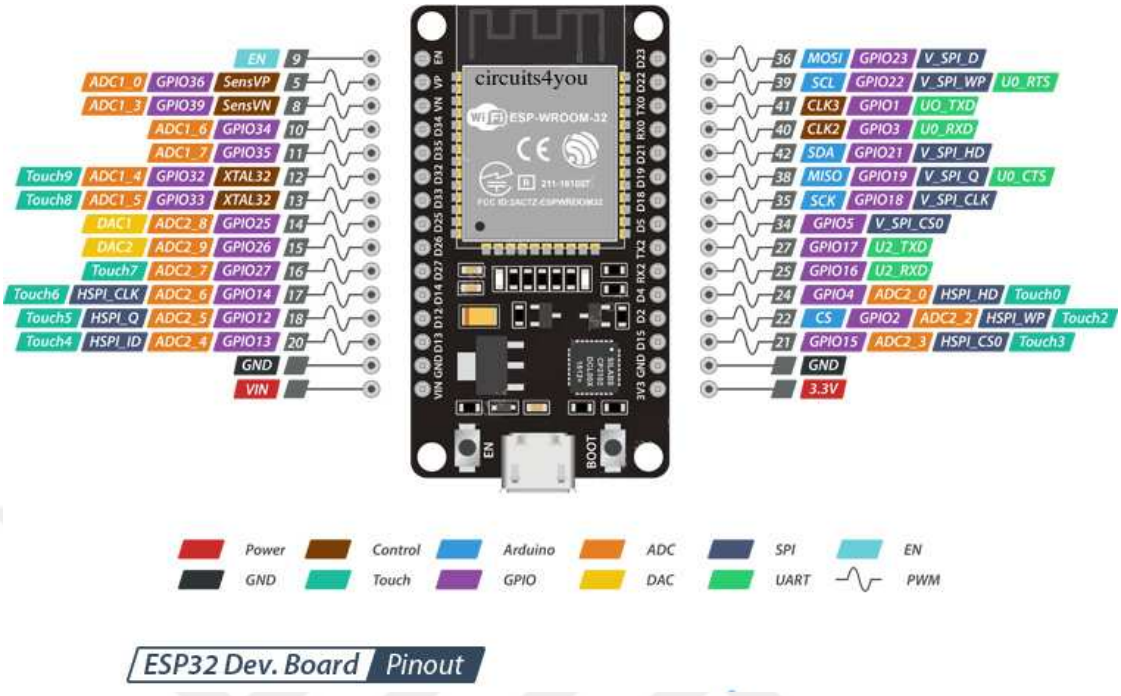

APPENDIX B: Microscanner Actuation Signal Code

```
1
2 //#define F 100 // 59.300 hz max
3 //#define FS (F*100)
4
5 int f=30;
6 float fs= 10000; //f*100
7
8 int sensorpin = 34;
9 int amp_count = 0;
10 int max_amplitude = 0;
11
12 #define inputPin 34 // ESP32 pin GIOP36 (ADC0) connected to Potentiometer
       pin
13
14 const int numReadings = 15;
15 int readings[numReadings];      // the readings from the analog input
16 int readIndex = 0;              // the index of the current reading
17 int total = 0;                  // the running total
18 int average = 0;
19
20  int max_av=0;
21  int min_av=10000;
22  long count = 0;
23  int max_ampl = 0;
24  int res_ampl = 0;
25
26 unsigned short sig[15000];//max 500Hz!!
27
28 float t ;
29 int i=0;
30
31  int num_period = 8; //number of periods applied
32  int period_count = 0; //period counter
33  int f_step = 1; //freq step
34
```

```
35
36 hw_timer_t * timer = NULL;
37 portMUX_TYPE timerMux = portMUX_INITIALIZER_UNLOCKED;
38
39 void IRAM_ATTR onTimer() {
40
41   portENTER_CRITICAL_ISR(&timerMux);
42
43   if( period_count < num_period){
44     if(i<=fs) i++;
45     else{
46       i=0;
47       period_count++;
48     }
49   }
50   else{
51     period_count = 0;
52     if( f < 140)
53       f += f_step;
54
55     fs = f*100;
56     unsigned int int_count = 1000000/fs;
57
58     timerAlarmWrite(timer, int_count, true);
59     //timerAlarmEnable(timer);
60   }
61   portEXIT_CRITICAL_ISR(&timerMux);
62
63 }
64 void setup() {
65
66   Serial.begin(115200);
67
68 float sensorValue = analogRead(sensorpin);
69
70   byte data = Serial.read();
71   if (data == 's')
```

```
72
73    // Serial.println(sensorValue);
74    //  delay(10);
75
76     for (int thisReading = 0; thisReading < numReadings; thisReading++) {
77     readings[thisReading] = 0;
78   }
79
80   f = 40;
81   fs = f*100;
82
83    timer = timerBegin(0, 80, true); //80Mhz/80=1MHz
84   timerAttachInterrupt(timer, &onTimer, true);
85   unsigned int int_count = 1000000/fs;
86
87   timerAlarmWrite(timer, int_count, true);
88   timerAlarmEnable(timer);
89
90   count = millis();
91
92 }
93 void loop() {
94
95   int analogValue = analogRead(inputPin); // read the input on analog pin
96
97   // subtract the last reading:
98   total = total - readings[readIndex];
99   // read from the sensor:
100  readings[readIndex] = analogRead(inputPin);
101  // add the reading to the total:
102  total = total + readings[readIndex];
103  // advance to the next position in the array:
104  readIndex = readIndex + 1;
105   // if we're at the end of the array...
106  if (readIndex >= numReadings) {
107    // ...wrap around to the beginning:
108    readIndex = 0;
```

```
109   }
110   // calculate the average:
111   average = total / numReadings ;
112   // send it to the computer as ASCII digits
113
114   if (average> max_av) max_av = average;
115
116   if (average < min_av)  min_av = average;
117
118
119
120   if( abs(max_av - min_av) > max_ampl){
121    max_ampl = abs(max_av - min_av);
122 //   Serial.println("Resonance");
123   }
124
125    if(millis() - count > 2000){
126      Serial.print("Max Ampl: ");
127     Serial.print(max_ampl);
128     Serial.print("  Res Ampl: ");
129     Serial.print(res_ampl);
130     Serial.print("  f: ");
131     Serial.println(f);
132
133     if (max_ampl>res_ampl)
134       res_ampl = max_ampl;
135
136     max_ampl = 0;
137     max_av = 0;
138     min_av=10000;
139     count = millis();
140
141
142   }
143
144   t=(float)i/fs;
145     sig[i]=( (short) (128.0 +2.0*(sin((2*f*PI*t)))));
```

```
146
147     dacWrite(25, sig[i]);
148
149 }
```

APPENDIX C: Microscanner Auto-Tuned Actuation Signal Code

```
1
2 //#define F 100 // 59.300 hz max
3 //#define FS (F*100)
4
5 int f=30;
6 float fs= 10000; //f*100
7
8 int sensorpin = 34;
9 int amp_count = 0;
10 int max_amplitude = 0;
11
12 #define inputPin 34 // ESP32 pin GIOP36 (ADC0) connected to Potentiometer
       pin
13
14 const int numReadings = 5;
15 int readings[numReadings];      // the readings from the analog input
16 int readIndex = 0;              // the index of the current reading
17 int total = 0;                  // the running total
18 int average = 0;
19 boolean can_measure = false;
20 boolean go_highestFreq = false;
21
22 //***********************************************
23
24
25 int currentIndex=0;
26 const int numMax = 5;
27 int max_ampl_1[numMax];
28 int currentMaxIndex = 0; // current index in the maximum array
29 int highestMax = 0; // highest maximum value found
30 int highestFreq = 0;
31
32
33 //***************************************************
```

```
34
35  int max_av=0;
36  int min_av=10000;
37  long count = 0;
38  int max_ampl = 0;
39  int res_ampl = 0;
40
41 unsigned short sig[15000];//max 500Hz!! 150hz max. 100*150
42
43 float t ;
44 int i=0;
45
46  int num_period = 2; //number of periods applied
47  int period_count = 0; //period counter
48  int f_step = 1; //freq step
49
50
51 hw_timer_t * timer = NULL;
52 portMUX_TYPE timerMux = portMUX_INITIALIZER_UNLOCKED;
53
54 void IRAM_ATTR onTimer() {
55
56   portENTER_CRITICAL_ISR(&timerMux);
57
58   if( period_count < num_period){
59     if(i<=fs) i++;
60     else{
61       i=0;
62       period_count++;
63     }
64   }
65   else{
66     period_count = 0;
67     if (go_highestFreq == false){
68       if( f < 100)
69         f += f_step;
70       else{
```

```
71          f= highestFreq-2;
72          go_highestFreq = true;
73          highestMax = 0;
74        }
75      }
76      else{
77        if( f < highestFreq + 2)
78          f += f_step;
79        else{
80          f= highestFreq-2;
81          highestMax = 0;
82        }
83      }
84      fs = f*100;
85      unsigned int int_count = 1000000/fs;
86
87      timerAlarmWrite(timer, int_count, true);
88      //timerAlarmEnable(timer);
89    }
90    portEXIT_CRITICAL_ISR(&timerMux);
91
92 }
93 void setup() {
94
95    Serial.begin(115200);
96
97 float sensorValue = analogRead(sensorpin);
98
99    byte data = Serial.read();
100   if (data == 's')
101
102     for (int thisReading = 0; thisReading < numReadings; thisReading++) {
103     readings[thisReading] = 0;
104   }
105
106
107 //*********************************************************
```

```
108     for (int thisReading = 0; thisReading < numMax; thisReading++) {
109    readings[thisReading] = 0;    }
110
111 //*********************************************************
112
113   f = 50;
114   fs = f*100;
115
116  timer = timerBegin(0, 80, true); //80Mhz/80=1MHz
117
118   timerAttachInterrupt(timer, &onTimer, true);
119   unsigned int int_count = 1000000/fs;
120
121   timerAlarmWrite(timer, int_count, true);
122   timerAlarmEnable(timer);
123
124   count = millis();
125
126 }
127 void loop() {
128
129   int analogValue = analogRead(inputPin); // read the input on analog pin
130
131   // subtract the last reading:
132   total = total - readings[readIndex];    // read from the sensor:
133
134   readings[readIndex] = analogRead(inputPin);
135
136   total = total + readings[readIndex]; // add the reading to the total:
137
138   readIndex = readIndex + 1;    // advance to the next position in the
      array:
139
140   if (readIndex >= numReadings) {    // if we're at the end of the array
      ...
141
142     readIndex = 0; // ...wrap around to the beginning:
```

```
143   }
144   average = total / numReadings ;  // calculate the average:
145
146   if (average> max_av) max_av = average;    // send it to the computer as
       ASCII digits
147
148   if (average < min_av)  min_av = average;
149
150   if( abs(max_av - min_av) > max_ampl){
151    max_ampl = abs(max_av - min_av);
152   }
153
154   //************************************************
155
156 if (can_measure){
157   max_ampl_1[currentMaxIndex] = max_ampl;
158   currentMaxIndex++;
159
160     if (currentMaxIndex == numMax) {
161       // find the highest Maximum
162
163       for (int i = 1; i < numMax; i++) {
164         if (max_ampl_1[i] > highestMax) {
165           highestMax = max_ampl_1[i];
166           highestFreq = f;
167         }
168       }
169
170       currentMaxIndex = 0;
171     }
172
173 }
174
175 //************************************************
176
177
178    if(millis() - count > 500){
```

```
179       Serial.print("Max Ampl: ");
180      Serial.print(max_ampl);
181 Serial.print(" Highest maximum: ");
182      Serial.println(highestMax);
183
184      Serial.print("  Highest Freq: ");
185      Serial.print(highestFreq);
186      Serial.print("  f: ");
187      Serial.println(f);
188
189
190    max_ampl = 0;
191    max_av = 0;
192    min_av=10000;
193    count = millis();
194    can_measure = true;
195
196
197   }
198
199   t=(float)i/fs;
200     sig[i]=( (short) (128.0 +8.0*(sin((2*f*PI*t)))));
201
202    dacWrite(25, sig[i]);
203
204
205    }
```

APPENDIX D: LDV Characterization MATLAB Code

```
1
2
3 clear all;
4 close all;
5 format long;
6
7 MIRROR_TYPE = 'Rect'; % Specify the mirror type to save it as a distinct
      file
8
9 % Reset signal generator
10 sg=gpib('ni',0,11); %ni: national instrument, ... index, primary adress
11 fopen(sg);
12 fprintf(sg,'*RST');
13
14 % Reset oscilloscope
15 os=gpib('ni',0,15);
16 fopen(os);
17 fprintf(os,'*RST');
18 fprintf(os,'SELECT:CONTROL CH2');
19
20 % Scanner dimension
21 D=3;
22
23 % Max amplitude value of the driving voltage of the actuator
24 amp = 1;
25
26 while(amp>0)
27
28 %%%%%%%%% Start and Stop Frequencies %%%%%%%%%%
29 startfreq = 70;
30 stopfreq = 300;
31
32 %%%%%%%%% Intermediate Freqencies and Step Sizes %%%%%%%%%%
33 FREQ(1)=115;
34 FREQ(2)=145;
```

```
35 %FREQ(3)=-160;
36 % FREQ(4)=190;
37 FREQ(3)=230;
38 FREQ(4)=250;
39 FREQ(5)=2000;
40 FREQ(6)=2110;
41
42 STEPPRECISE=1;
43 STEPWIDE=5;
44 SETTLEWAIT=1;
45 fstep=0;
46
47 %%%%%%%%% Automatic horizontal scale flags %%%%%%%
48 done1=0;
49 done2=0;
50 done3=0;
51 done4=0;
52 done5=0;
53 done6=0;
54
55 % Initiliaze signal generator for measurement
56 fprintf(sg,'FUNC SIN');                                    % Couldn't find
       this code in the reference!
57
58 %fprintf(sg,'VOLT:UNIT VPP');
59 fprintf(sg,['SOUR1:VOLT:AMPL ',num2str(amp)]);             % Set voltage
       amplitute
60 fprintf(sg,['SOUR1:FREQ:FIX ',num2str(startfreq)]);       % Set the
       starting frequency
61 fprintf(sg,'OUTP:STAT ON')                                % Set sg output
       channel to ON
62
63 % initiliaze oscilloscope for measurement
64 fprintf(os,'MEASUREMENT:IMMED:SOURCE CH1');
65 fprintf(os,'MEASUREMENT:IMMED:SOURCE2 CH2');
66 fprintf(os,'AUTOSET EXECUTE');                             % Execute autoset
       command
```

```
67 pause(1);
68 fprintf(os,'CH1:POS 0');
69 fprintf(os,'CH2:POS 0');
70 pause(1);
71
72 %%%%%%%%% 10 secs for manual configuration of oscilloscope %%%%%%%%%%
73 fsp=0;
74 i= startfreq;
75 resonant_frequency=0;
76 vel_temp=0;
77 count = 1;
78
79 while( i < stopfreq)
80
81 %%%%%%%%% Set steps for intermediate frequencies %%%%%%%%%%
82     if( i>= FREQ(2*fsp+1))
83         if( i <= FREQ(2*fsp+2) )
84             fstep=STEPPRECISE;
85             SETTLEWAIT=0.5;
86         else
87             fsp=fsp+1;
88             fstep=STEPWIDE;
89             SETTLEWAIT=0.5;
90         end
91     else
92        fstep=STEPWIDE;
93        SETTLEWAIT=0.5;
94     end
95
96     % Oscilloscope adjustments: set horizontal timing scale
97      if( i < 50 )
98          if(done1==0)
99              fprintf(os,'HORIZONTAL:SCALE 0.02');
100             pause(1);
101             done1=1;
102         end
103      else
```

```
104
105
106             if(i<160)
107                 if(done2==0)
108                     fprintf(os,'HORIZONTAL:SCALE 0.004');
109                     pause(1);
110                     done2=1;
111                 end
112             else
113
114                  if(i<280)
115                      if(done3==0)
116                          fprintf(os,'HORIZONTAL:SCALE 0.002');
117                          pause(1);
118                          done3=1;
119                      end
120                  else
121
122                      if(i<800)
123                          if(done4==0)
124                              fprintf(os,'HORIZONTAL:SCALE 0.001');
125                              pause(1);
126                              done4=1;
127                          end
128                      else
129
130                           if(i<1500)
131                              if(done5==0)
132                                  fprintf(os,'HORIZONTAL:SCALE 0.0004');
133                                  pause(1);
134                                  done5=1;
135                              end
136                           else
137
138                              if(i<2000)
139                                  if(done6==0)
140                                      fprintf(os,'HORIZONTAL:SCALE 0.0002');
```

```
141                                     pause(1);
142                                     done6=1;
143                                 end
144                             end
145                         end
146                     end
147                 end
148             end
149         end
150
151         fprintf(sg,['SOUR1:FREQ:FIX ',num2str(i)]);      % Update frequency
152         pause(SETTLEWAIT);                               % wait for scanner to
            settle
153
154         %%%%%%%%% Sampling for one step %%%%%%%%%%
155         N = 5;
156         temppk2pk = zeros(1,N);
157         %temppha = zeros(1,N);
158
159         for j = 1:N
160             temppk2pk(j)= 0;
161             % temppha(j)  = 0;
162             % Measure duty-cycle N times
163             fprintf(os,'MEASUREMENT:IMMED:TYPE PK2PK');
164             fprintf(os,'MEASUREMENT:IMMED:VALUE?');
165             temppk2pk(j) = fscanf(os,'%f'); %Read p2p value of the output
            signal. (1V per 100mm/s)
166         end
167
168         vel(count) = mean(temppk2pk); %Average of the N measurements
169
170         %%%%%%%%%% If this frequency is higher than older ones then this is
            the resonant frequency %%%%%%%%%%
171         if ( vel(count) > vel_temp )
172             vel_temp = vel(count);
173             resonant_frequency = num2str(i);
174         end
```

```
175
176     %%%%%%%% Automation ( BETA ) %%%%%%%%%%
177     if( vel(count) < 0.04)
178         fprintf(os,'CH1:SCALE 0.01');
179             pause(1);
180     else
181         if( vel(count) < 0.081)
182             fprintf(os,'CH1:SCALE 0.02');
183             pause(1);
184         else
185             if ( vel(count) < 0.21)
186                 fprintf(os,'CH1:SCALE 0.05');
187                 pause(1);
188             else
189                 if ( vel(count) < 0.41)
190                    fprintf(os,'CH1:SCALE 0.1');
191                    pause(1);
192                 else
193                     if ( vel(count) < 0.81)
194                         fprintf(os,'CH1:SCALE 0.2');
195                         pause(1);
196                     else
197                         if ( vel(count) < 2.1)
198                             fprintf(os,'CH1:SCALE 0.5');
199                             pause(1);
200                         else
201                             if ( vel(count) < 4.1)
202                                 fprintf(os,'CH1:SCALE 1.0');
203                                 pause(1);
204                             else
205                                 if ( vel(count) < 8.1)
206                                     fprintf(os,'CH1:SCALE 2.0');
207                                     pause(1);
208                                 else
209                                     if ( vel(count) < 20.1)
210                                         fprintf(os,'CH1:SCALE 5.0');
211                                         pause(1);
```

```
212                                         end
213                                     end
214                                 end
215                             end
216                         end
217                     end
218                 end
219             end
220         end
221
222         %pha(count) = mean(temppha);
223         ref(count) = i;
224         count = count + 1;
225         pause(0.1);
226
227         i=i+fstep;  %Update the current value of the freq. to the next freq.
            value
228 end
229
230 save([MIRROR_TYPE '_Amp' num2str(amp)]);                %Save all the
        datas of the corresponding mirror with the associated amplitude value
231 save([MIRROR_TYPE 'Plot_Data_Amp' num2str(amp)],'vel') %Save the velocity
         values that comes from the ldv while the amp. value of the driving
        signal of the coil is equal to amp.
232 pause(1);
233 figure,plot(ref,vel);
234 xlabel('Frequency [Hz]');
235 ylabel('Magnitude [V_{pp}]');
236 pause(1);
237 amp=amp-1;
238 end
239
240 %reset all devices and close the gpib session
241 fprintf(sg,'*RST');
242 fprintf(os,'*RST');
243 fclose(sg);
244 fclose(os);
```

```
245 clear sg;
246 clear os;
247
248 %     disp1=vel*100;
249 %     for J=1:length(ref)
250 %         disp(J)=disp1(J)/(6.14*ref(J));
251 %         theta_radian(J)=2*asin(disp(J)/D);
252 %         theta(J)=theta_radian(J)*180/pi;
253 %         thetaDproduct(J)=theta(J)*D;
254 %     end
255
256 % plot(ref,disp);
257 % xlabel('Frequency [Hz]');
258 % ylabel('Displacement [mm]');
259 %figure,plot(ref,theta);
260 %xlabel('Frequency [Hz]');
261 %ylabel('Angle of Displacement [deg]');
262 %figure,plot(ref,thetaDproduct);
263 %xlabel('Frequency [Hz]');
264 %ylabel('Theta*D product [deg.mm]');
265
266 %figure, plot(ref,pha);
267 %xlabel('Frequency [Hz]');
268 %ylabel('Phase [deg]');
```